CRB Optimization for Intelligent Reflecting Surface-Assisted NLOS Wireless Sensing

Jilin Wang, Jun Fang, Hongbin Li, *Fellow, IEEE*, and Christos Masouros, *Fellow, IEEE*

***Abstract*—In this paper, we investigate an intelligent reflecting surface (IRS)-assisted non-line-of-sight (NLOS) wireless sensing system, where an IRS aids an access point (AP) in estimating the parameters of a target in its NLOS region. The AP transmits signals and detects the target based on echoes propagating through the AP-IRS-target-IRS-AP channel. A key challenge in IRS-assisted NLOS sensing is the inherent scaling ambiguity, which arises when the degrees of freedom (DoFs) provided by the AP-IRS channel are insufficient to uniquely estimate both the complex path gain and angular parameters of the target. To address this issue, we introduce a two-stage sensing scheme that leverages the diversity of the IRS illumination pattern. Within this framework, we derive a compact Cramér-Rao Bound (CRB) expression for direction-of-arrival (DOA) estimation, enabling the decoupled optimization of the AP's transmit beamformer and IRS phase shifts via CRB minimization. Specifically, the optimal beamformer is obtained in a closed form, while the IRS reflective coefficients are optimized using a majorization-minimization (MM)-based algorithm. Simulation results demonstrate the superiority of the proposed method, achieving lower CRB and MSE compared to benchmark schemes, particularly in challenging scenarios where the AP-IRS channel DoFs are insufficient to resolve the scaling ambiguity.**

***Index terms*—** Intelligent reflecting surface (IRS), NLOS wireless sensing, Cramér-Rao Bound (CRB), transmit beamformer design, IRS reflective coefficients optimization.

I. Introduction

A. Background

The integration of wireless sensing into communication networks has become a defining trend in beyond fifth-generation (B5G) and sixth-generation (6G) systems, enabling applications such as autonomous navigation, smart cities, and industrial automation [1]–[4]. Conventional sensing techniques, including radar-based detection, received signal strength (RSS)-based localization, and time-of-arrival (TOA) estimation, typically rely on the presence of line-of-sight (LOS) propagation between the radar/access point (AP) and the target. However, in practical environments, such as dense urban areas, indoor settings, and military scenarios, LOS paths are often obstructed, leading to severe degradation in sensing and localization accuracy.

To overcome this limitation, intelligent reflecting surface (IRS) technology has emerged as a cost-effective and energy-efficient solution for enhancing wireless sensing, communications, and localization [5]–[10]. An IRS consists of a linear/planar array of passive reflective elements that dynamically adjust phase shifts to reconfigure the wireless environment, enabling signal redirection and virtual LOS link creation without the need for additional active APs. By leveraging IRS, non-line-of-sight (NLOS) targets can be detected through controlled reflections along the AP-IRS-target-IRS-AP propagation path. However, severe signal attenuation over multi-hop reflections remains a key challenge, necessitating intelligent IRS phase shift optimization to maximize reflected signal strength and enhance sensing performance [11]–[27].

B. Related Work

There have been extensive works investigating IRS-assisted wireless sensing system, encompassing IRS-aided radar for target detection and parameter estimation [11]–[23], and IRS-assisted integrated sensing and communication (ISAC) systems [24]–[27].

For IRS-aided target detection in NLOS system, the study in [11] formulated an IRS-aided multi-input multi-output (MIMO) radar detection problem. In this framework, the IRS is positioned near the radar transmitter or receiver to enhance the illumination or observation of potential targets. An IRS-assisted radar system for target surveillance in a cluttered environment was investigated in [12]. In this work, the active beamformer at the radar transmitter and the passive phase-shift matrices at the IRSs were jointly optimized to maximize the minimum target illumination power across multiple target locations. The moving target detection problem in a multi-IRS-aided orthogonal frequency division multiplexing (OFDM) radar system was addressed in [13], where a bi-quadratic program was derived to jointly design the OFDM signal and IRS phase shifts for optimizing target detection performance.

In addition to target detection, the problem of parameter estimation in IRS-aided systems has also been extensively investigated. In [14], a generalized likelihood ratio test (GLRT) based detector and a repetitive IRS phase profile were developed for an IRS-aided monostatic sensing system, with the 2D unitary ESPRIT method employed to efficiently retrieve target parameters. In [15], an IRS-self-sensing architecture is proposed, in which the IRS controller transmits probing

Jilin Wang is with the National Key Laboratory of Wireless Communications, University of Electronic Science and Technology of China, Chengdu 611731, China, also with the Department of Electronic and Electrical Engineering, University College London, WC1E 7JE London, U.K. (e-mail: jilinwang@std.uestc.edu.cn).

Jun Fang is with the National Key Laboratory of Wireless Communications, University of Electronic Science and Technology of China, Chengdu 611731, China (e-mail: JunFang@uestc.edu.cn)

Hongbin Li is with the Department of Electrical and Computer Engineering, Stevens Institute of Technology, Hoboken, NJ 07030, USA (e-mail: Hongbin.Li@stevens.edu).

Christos Masouros is with the Department of Electronic and Electrical Engineering, University College London, WC1E 7JE London, U.K. (e-mail: c.masouros@ucl.ac.uk).

This article has been accepted for publication in IEEE Transactions on Signal Processing. This is the author's version which has not been fully edited and content may change prior to final publication. Citation information: DOI 10.1109/TSP.2025.3609719

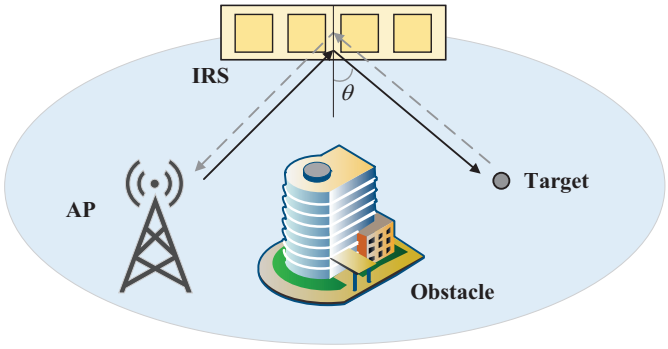

Fig. 1: Illustration of the considered IRS-assisted NLOS sensing system.

signals, and dedicated sensors at the IRS perform location and angle estimation based on echo signals received via the BS-IRS-target-IRS sensor link and the BS-target-IRS sensor link. The problem of NLOS sensing, encompassing both target detection and parameter estimation, was investigated in [16], [17]. The work in [16] focused on an IRS-enabled pulse-Doppler radar system, deriving the minimum variance for the best linear unbiased estimator (BLUE) of the target backscattering coefficient and optimizing IRS phase shifts to minimize the mean squared error of the estimated target parameters. Meanwhile, [17] proposed a hierarchical three-dimensional (3D) IRS beam training approach, where an initial coarse target detection and direction estimation phase was followed by fine-grained sensing, refining the estimates of target ranges and velocities by steering IRS beams toward detected targets. Furthermore, [18] examined a backward IRS-aided MIMO radar system and proposed a reduced-dimension multiple signal classification (MUSIC) estimator for joint direction-of-departure (DOD) and direction of arrival (DOA) estimation. However, this study assumed a fixed IRS phase-shift profile with binary phase shifts (0 and π). In [19], the authors proposed a two-stage sensing scheme for IRS-aided NLOS system, where the received OFDM signals in the two stages were represented as two third-order tensors, enabling a tensor decomposition-based approach for estimating DOAs, time delays, and Doppler shifts of targets.

Beyond algorithmic approaches, NLOS parameter estimation has also been studied from a theoretical perspective by analyzing the Cramér-Rao Bound (CRB) performance, leading to IRS coefficient design via CRB optimization. Specifically, [20] investigated DOA estimation in an IRS-enabled NLOS sensing system, where transmit and reflective beamforming were jointly optimized to minimize the CRB for target parameter estimation, demonstrating enhanced sensing accuracy for both point and extended target models. Extending this methodology, the authors in [21] investigated a multi-IRS-assisted MIMO radar system, while [22] considered a semi-passive IRS-enabled sensing setup, both further demonstrating the effectiveness of CRB-based optimization in complex NLOS environments.

Despite these advancements, most existing IRS-assisted sensing studies have not explicitly addressed the inherent scaling ambiguity issue. As pointed out in [20] and further emphasized in [23], when the rank of the AP-IRS channel matrix is one, at least two degrees-of-freedom (DoFs) are required to simultaneously identify both the complex path gain and the angular parameter of the target, otherwise a scaling ambiguity arises. To mitigate this issue, [19] proposed a two-stage sensing scheme, leveraging the diversity of the IRS illumination pattern across the two stages. However, the subarray partition-based IRS phase shift design introduced in [19] is an empirical approach that leads to noticeable performance degradation.

Motivated by these limitations, this paper investigates an IRS-assisted sensing system, where the AP transmits sensing signals and estimates the target parameters based on echo signals propagating through the AP-IRS-target-IRS-AP channel. To address the scaling ambiguity inherent in IRS-assisted sensing, we adopt the two-stage sensing scheme originally proposed in [19]. Note the work [19] is only concerned about developing an estimation algorithm for IRS-assisted NLOS sensing problems. The joint optimization of the AP's transmit beamformer and IRS phase shifts was not studied in [19]. Unlike [19] which primarily addresses algorithm development, this paper focuses on optimizing the transmit beamformer as well as the IRS's reflection coefficients to maximize the sensing performance. Our work introduces a new CRB minimization approach for IRS phase shift optimization within the two-stage scheme. This represents a significant advancement beyond the empirical IRS design methods used in [19]. Specifically, we derive a succinct CRB expression for DOA estimation, which enables the decomposition of the joint optimization problem into two sub-problems: transmit beamformer design and IRS phase shift optimization. Based on this formulation, we minimize the CRB for parameter estimation by jointly optimizing the AP transmit beamformer and IRS reflective coefficients, thereby enhancing sensing accuracy and robustness.

The remainder of this paper is organized as follows. Section II introduces the system model as well as the two-stage scheme based signal model. Section III formulates a succinct expression for the estimation CRB. Section IV minimizes the CRB for estimating DOA by jointly optimizing the transmit beamforming at the AP and the reflective coefficients at the IRS. Section V introduces a practical maximum likelihood estimation (MLE) method to estimate the target's DOA. Simulation results are presented in Section VI, followed by concluding remarks in Section VII.

Notations: In this paper, scalars, column vectors, matrices and tensors are denoted by italic, lowercase boldface, uppercase boldface and calligraphic boldface letters, respectively. $[\boldsymbol{a}]_i$, $[\boldsymbol{A}]_{i,l}$, denote the ith element of $\boldsymbol{a}$ and the (i,l)th element of $\boldsymbol{A}$, respectively. $\mathrm{rank}(\boldsymbol{A})$ and $\mathrm{tr}(\boldsymbol{A})$ denote the rank of $\boldsymbol{A}$ and the trace of $\boldsymbol{A}$, respectively. The operator $\mathrm{diag}(\boldsymbol{a})$ denotes a diagonal matrix whose main diagonal elements are the elements of the vector $\boldsymbol{a}$. Conversely, $\mathrm{diag}(\boldsymbol{A})$ extracts the main diagonal elements of $\boldsymbol{A}$ and forms a column vector $\boldsymbol{a}$. $\boldsymbol{I}_M$ denotes the identity matrix of size M. The symbols $(\cdot)^*$, $(\cdot)^T$, $(\cdot)^H$, $(\cdot)^{-1}$, denote the conjugate, transpose, conjugate transpose, and inverse, respectively. $\|\cdot\|_2$ and $\|\cdot\|_F$ denote

the 2-norm and Frobenius norm, respectively. j denotes the imaginary unit. $\Re\{\cdot\}$ and $\Im\{\cdot\}$ denote the real and imaginary parts of a complex number, respectively.

II. Problem Formulation

A. System Model

We consider an IRS-assisted wireless sensing system as shown in Fig.1, which is employed to locate a target in the NLOS area of the access point (AP). Suppose both the AP and the IRS are equipped with a uniform linear array (ULA), with M antennas at the AP and N elements at the IRS. The AP transmits a sensing signal and then perceives the target based on the echo signal propagating through the AP-IRS-target-IRS-AP channel.

Define $\boldsymbol{G} \in \mathbb{C}^{N\times M}$ as the channel matrix from the AP to the IRS. Since the positions of the AP and the IRS are predetermined, we assume that the AP perfectly knows the channel matrix $\boldsymbol{G}$ of the AP-IRS link. Each element on the IRS can combine the incident signal and then re-scatter the combined signal with a certain phase shift. Define $\psi_n \in [0, 2\pi]$ as the phase shift associated with the nth passive element of the IRS. Also, the associated reflection matrix at IRS can be expressed as

$$\boldsymbol{\Phi} = \mathrm{diag}(e^{j\psi_1}, \cdots, e^{j\psi_N}). \tag{1}$$

Define θ as a target's direction-of-arrival (DOA) with respect to the IRS. The associated steering vector at the IRS can be written as

$$\boldsymbol{a}(\theta) = [1 \;\; e^{j2\pi\frac{d\sin(\theta)}{\lambda}} \;\; \cdots \;\; e^{j2\pi\frac{(N-1)d\sin(\theta)}{\lambda}}]^T, \tag{2}$$

where d denotes the spacing between any two adjacent reflection elements, and λ is the wavelength of the carrier signal. For the target, the cascaded IRS-target-IRS channel can be written as

$$\boldsymbol{H} = \alpha\boldsymbol{a}(\theta)\boldsymbol{a}^T(\theta), \tag{3}$$

where $\alpha \in \mathbb{C}$ is used to characterize the effective path gain, which indicates the round-trip path loss as well as the radar cross section (RCS) coefficient of the target.

B. Signal Model

Let $s(t)$ and $\boldsymbol{w} \in \mathbb{C}^M$ denote the transmitted signal at time instant t and the beamforming vector, respectively. Then the transmitted signal is expressed as $\boldsymbol{x}(t) = \boldsymbol{w}s(t)$, where $|s(t)|^2 = 1$. Also, a transmit power constraint is placed on the beamforming vector $\boldsymbol{w}$, i.e. $\|\boldsymbol{w}\|_2^2 \le P_T$, P_T is the transmit power. In a coherent processing interval (CPI), the AP transmits radio signals and then receives the echo from the potential target via the AP-IRS-target-IRS-AP link. The received echo signal at the AP at time t can be expressed as

$$\boldsymbol{y}(t) = \boldsymbol{G}^T\boldsymbol{\Phi}^T\boldsymbol{H}\boldsymbol{\Phi}\boldsymbol{G}\boldsymbol{w}s(t) + \boldsymbol{n}(t), \tag{4}$$

where $\boldsymbol{n}(t)$ denotes the additive noise. Note when the AP-IRS channel is rank-one or approximately rank-one, there exists an inherent scaling ambiguity for estimating the DOA from the received signals [20]. Specifically, when $\mathrm{rank}(\boldsymbol{G}) = 1$, the channel matrix can be expressed as $\boldsymbol{G} = \sigma\boldsymbol{p}\boldsymbol{q}^H$, where σ is a scaling factor, and $\boldsymbol{p} \in \mathbb{C}^N$, $\boldsymbol{q} \in \mathbb{C}^M$ are the channel response vectors. Consequently, the received echo signal in (4) at the AP can be further written as

$$\boldsymbol{y}(t) = \alpha\sigma^2\boldsymbol{q}^*\underbrace{\boldsymbol{p}^T\boldsymbol{\Phi}^T\boldsymbol{a}(\theta)\boldsymbol{a}^T(\theta)\boldsymbol{\Phi}\boldsymbol{p}}_{\beta(\theta)}\underbrace{\boldsymbol{q}^H\boldsymbol{w}s(t)}_{\tilde{\boldsymbol{x}}(t)} + \boldsymbol{n}(t), \tag{5}$$

where $\beta(\theta) = \boldsymbol{p}^T\boldsymbol{\Phi}^T\boldsymbol{a}(\theta)\boldsymbol{a}^T(\theta)\boldsymbol{\Phi}\boldsymbol{p}$ is the only term related to θ. Notice that α and $\beta(\theta)$ are coupled in (5). Owing to the coupling, the parameter θ in (5) can not be uniquely identified. This will also be interpreted from the CRB perspective later.

To avoid the inherent scaling ambiguity in the IRS-assisted NLOS sensing system, we employ the two-stage sensing scheme which was first proposed in [19]. Accordingly, let $\boldsymbol{\Phi}_i \in \mathbb{C}^{N\times N}$ denotes the individual IRS phase-shift matrix in stage $i \in \{1, 2\}$. Then, the received signal at stage i is given by

$$\begin{aligned}\boldsymbol{y}_i(t) &= \boldsymbol{G}^T{\boldsymbol{\Phi}_i}^T\boldsymbol{H}\boldsymbol{\Phi}_i\boldsymbol{G}\boldsymbol{w}s(t) + \boldsymbol{n}_i(t)\\ &= \alpha\boldsymbol{G}^T{\boldsymbol{\Phi}_i}^T\boldsymbol{a}(\theta)\boldsymbol{a}^T(\theta)\boldsymbol{\Phi}_i\boldsymbol{G}\boldsymbol{w}s(t) + \boldsymbol{n}_i(t)\\ &= \alpha\boldsymbol{b}_i(\theta)\boldsymbol{b}_i^T(\theta)\boldsymbol{w}s(t) + \boldsymbol{n}_i(t),\end{aligned} \tag{6}$$

where $\boldsymbol{b}_i(\theta) \triangleq \boldsymbol{G}^T{\boldsymbol{\Phi}_i}^T\boldsymbol{a}(\theta) \in \mathbb{C}^M$ denotes the effective steering vector, and $\boldsymbol{n}_i(t) \in \mathbb{C}^M \sim \mathcal{CN}(\boldsymbol{0}, \sigma_i^2\boldsymbol{I}_M)$ denotes the additive noise, where σ_i^2 is the noise power for stage i. The two-stage sensing scheme utilizes the corresponding observations to estimate the DOA parameter. As discussed in [19], this scheme relies on the diversity of the IRS illumination patterns across the two stages, requiring that the IRS beams in both stages simultaneously illuminate the target while maintaining sufficient pattern diversity. However, quantifying and optimizing the illumination diversity between the two stages is highly challenging, making the derivation of optimal IRS phase matrices a nontrivial task. To address this challenge, this paper proposes a CRB-based analytical framework, which provides a systematic and efficient approach to optimize the IRS phase matrices for the two-stage sensing scheme, ensuring robust parameter estimation performance.

III. CRB Analysis

In this section, we analyze the estimation performance. We derive a succinct expression for the estimation CRB, which decouples the transmit beamformer and the IRS reflective coefficients.

Consider the CRB for estimating the DOA θ from the two-stage observations over the radar dwell time, e.g., $\{\boldsymbol{y}_i(t)\}$, $i \in \{1, 2\}$ and $t = 1, 2\cdots, T$. Then, we stack the received signals as

$$\boldsymbol{Y}_i = \alpha\boldsymbol{b}_i(\theta)\boldsymbol{b}_i^T(\theta)\tilde{\boldsymbol{X}} + \boldsymbol{N}_i, \tag{7}$$

where $\boldsymbol{Y}_i = [\boldsymbol{y}_i(1) \;\cdots\; \boldsymbol{y}_i(T)] \in \mathbb{C}^{M\times T}$, $\tilde{\boldsymbol{X}} \triangleq [\boldsymbol{w}s(1) \;\cdots\; \boldsymbol{w}s(T)] \in \mathbb{C}^{M\times T}$, and $\boldsymbol{N}_i \triangleq [\boldsymbol{n}_i(1) \;\cdots\; \boldsymbol{n}_i(T)] \in \mathbb{C}^{M\times T}$, respectively. To

further understand the two-stage sensing scheme, we define $\boldsymbol{Y} \triangleq [\boldsymbol{Y}_1 \ \boldsymbol{Y}_2] \in \mathbb{C}^{M\times 2T}$, and we have

$$\begin{aligned}\boldsymbol{Y} &= \alpha[\boldsymbol{b}_1(\theta)\boldsymbol{b}_1^T(\theta)\tilde{\boldsymbol{X}} \ \ \boldsymbol{b}_2(\theta)\boldsymbol{b}_2^T(\theta)\tilde{\boldsymbol{X}}] \\ &= \alpha[\boldsymbol{b}_1(\theta) \ \ \boldsymbol{b}_2(\theta)]\begin{bmatrix} \boldsymbol{b}_1^T(\theta) & \\ & \boldsymbol{b}_2^T(\theta)\end{bmatrix}\begin{bmatrix}\tilde{\boldsymbol{X}} & \\ & \tilde{\boldsymbol{X}}\end{bmatrix} + \boldsymbol{N} \\ &= \alpha\boldsymbol{B}(\theta)\boldsymbol{C}^T(\theta)\boldsymbol{X} + \boldsymbol{N} \\ &= \alpha\boldsymbol{Q}(\theta)\boldsymbol{X} + \boldsymbol{N}, \end{aligned} \tag{8}$$

where $\boldsymbol{B}(\theta) \triangleq [\boldsymbol{b}_1(\theta) \ \boldsymbol{b}_2(\theta)] \in \mathbb{C}^{M\times 2}$, $\boldsymbol{C}(\theta) \triangleq \text{blkdiag}(\boldsymbol{b}_1(\theta), \boldsymbol{b}_2(\theta)) \in \mathbb{C}^{2M\times 2}$, $\boldsymbol{Q}(\theta) \triangleq \boldsymbol{B}(\theta)\boldsymbol{C}^T(\theta) \in \mathbb{C}^{M\times 2M}$, $\boldsymbol{X} \triangleq \text{blkdiag}(\tilde{\boldsymbol{X}}, \tilde{\boldsymbol{X}}) \in \mathbb{C}^{2M\times 2T}$, and $\boldsymbol{N} \triangleq [\boldsymbol{N}_1 \ \boldsymbol{N}_2] \in \mathbb{C}^{M\times 2T}$.

Let $\boldsymbol{\zeta} \triangleq [\theta \ \boldsymbol{\alpha}^T]^T \in \mathbb{R}^3$ denotes the vector of unknown parameters to be estimated, where θ represents the target's DOA with respect to the IRS, and $\boldsymbol{\alpha} = [\Re\{\alpha\}, \Im\{\alpha\}]^T$ represents the complex-valued effective path gain. For notational brevity, in the following discussion, we denote $\boldsymbol{Q}(\theta)$, $\boldsymbol{B}(\theta)$, $\boldsymbol{C}(\theta)$, $\boldsymbol{a}(\theta)$ as $\boldsymbol{Q}$, $\boldsymbol{B}$, $\boldsymbol{C}$ and $\boldsymbol{a}$, respectively. By vectorizing (8), we have

$$\tilde{\boldsymbol{y}} = \text{vec}(\boldsymbol{Y}) = \boldsymbol{z} + \boldsymbol{n}, \tag{9}$$

where $\boldsymbol{z} = \alpha\text{vec}(\boldsymbol{Q}\boldsymbol{X})$ and $\boldsymbol{n} = \text{vec}(\boldsymbol{N}) \sim \mathcal{CN}(\boldsymbol{0}, \sigma_N^2\boldsymbol{I}_{2MT})$. Let $\boldsymbol{J} \in \mathbb{R}^{3\times 3}$ denote the FIM for estimating $\boldsymbol{\zeta}$. Based on [20], the FIM $\boldsymbol{J}$ can be partitioned as

$$\boldsymbol{J} = \begin{bmatrix} \boldsymbol{J}_{\theta\theta} & \boldsymbol{J}_{\theta\alpha} \\ \boldsymbol{J}_{\theta\alpha}^T & \boldsymbol{J}_{\alpha\alpha}\end{bmatrix}, \tag{10}$$

where

$$\boldsymbol{J}_{\theta\theta} = \frac{2T|\alpha|^2}{\sigma_N^2}\text{tr}(\dot{\boldsymbol{Q}}\boldsymbol{R}_x\dot{\boldsymbol{Q}}^H), \tag{11}$$

$$\boldsymbol{J}_{\theta\alpha} = \frac{2T}{\sigma_N^2}\Re\{\alpha^*\text{tr}(\boldsymbol{Q}\boldsymbol{R}_x\dot{\boldsymbol{Q}}^H)[1,j]\}, \tag{12}$$

$$\boldsymbol{J}_{\alpha\alpha} = \frac{2T}{\sigma_N^2}\text{tr}(\boldsymbol{Q}\boldsymbol{R}_x\boldsymbol{Q}^H)\boldsymbol{I}_2, \tag{13}$$

where $\boldsymbol{R}_x = \frac{1}{T}\boldsymbol{X}\boldsymbol{X}^H \in \mathbb{C}^{2M\times 2M}$ and $\dot{\boldsymbol{Q}}$ denotes the partial derivation of $\boldsymbol{Q}$ w.r.t. θ.

The CRB for estimating the DOA θ corresponds to the first diagonal element of the inverse Fisher Information Matrix (FIM), i.e.,

$$\text{CRB}(\theta) = [\boldsymbol{J}^{-1}]_{1,1} = [\boldsymbol{J}_{\theta\theta} - \boldsymbol{J}_{\theta\alpha}\boldsymbol{J}_{\alpha\alpha}^{-1}\boldsymbol{J}_{\theta\alpha}^T]^{-1}. \tag{14}$$

Based on equations (10)-(14), we have the following lemma.

Lemma 1. *The CRB for DOA θ estimation can be expressed as*

$$\text{CRB}(\theta) = \frac{\sigma_N^2}{2T|\alpha|^2\left(\text{tr}(\dot{\boldsymbol{Q}}\boldsymbol{R}_x\dot{\boldsymbol{Q}}^H) - \frac{|\text{tr}(\boldsymbol{Q}\boldsymbol{R}_x\dot{\boldsymbol{Q}}^H)|^2}{\text{tr}(\boldsymbol{Q}\boldsymbol{R}_x\boldsymbol{Q}^H)}\right)}. \tag{15}$$

Note that this CRB expression is general and applies to any channel matrix of the AP-IRS link. To gain deeper insight into this expression and to facilitate the design of IRS reflective beamforming for the two-stage sensing scheme under the rank-one condition for the AP-IRS channel matrix, we now reformulate $\text{CRB}(\theta)$ in (15) in terms of the IRS reflective coefficients. Specifically, If the AP-IRS channel is rank-one, it can be expressed as $\boldsymbol{G} = \sigma\boldsymbol{p}\boldsymbol{q}^H$, where $\boldsymbol{p} \in \mathbb{C}^N$ and $\boldsymbol{q} \in \mathbb{C}^M$ are the channel response vectors. Define $\boldsymbol{D} \triangleq \text{diag}(0, 1\cdots, N-1) \in \mathbb{C}^{N\times N}$, $\boldsymbol{A} \triangleq \text{diag}(\boldsymbol{a}(\theta)) \in \mathbb{C}^{N\times N}$ and $\boldsymbol{\psi}_i \triangleq \text{diag}(\boldsymbol{\Phi}_i) \in \mathbb{C}^N, i \in \{1,2\}$. Accordingly we have the following lemma.

Lemma 2. *If the AP-IRS channel is rank-one, then the CRB for DOA θ estimation is given by* (16)*, shown at the top of next page, where $\mu_i \triangleq \boldsymbol{\psi}_i^H\boldsymbol{F}\boldsymbol{\psi}_i$, $\bar{\mu}_i \triangleq \boldsymbol{\psi}_i^H\boldsymbol{D}\boldsymbol{F}\boldsymbol{D}\boldsymbol{\psi}_i$ and $\tilde{\mu}_i \triangleq \boldsymbol{\psi}_i^H\boldsymbol{D}\boldsymbol{F}\boldsymbol{\psi}_i$, $i \in \{1,2\}$, with $\boldsymbol{F} \triangleq \boldsymbol{A}^H\boldsymbol{p}^*\boldsymbol{p}^T\boldsymbol{A}$.*

Proof. See Appendix A. □

In the CRB expression (16), note that the terms

$$(\mu_1\bar{\mu}_1 + \mu_2\bar{\mu}_2) - \frac{|\mu_1\tilde{\mu}_1 + \mu_2\tilde{\mu}_2|^2}{|\mu_1|^2 + |\mu_2|^2}, \tag{17}$$

and $|\boldsymbol{q}^H\boldsymbol{w}|^2$ are respectively related to the IRS reflective coefficients and transmit beamformer. This compact formulation is useful for the joint design of the transmit beamformer and IRS reflective beamforming through CRB minimization. Furthermore, the following proposition underscores the importance of using different IRS phase-shift matrices across the two sensing stages.

Proposition 1. *If the AP-IRS channel is rank-one (i.e., $\text{rank}(\boldsymbol{G}) = 1$) and the IRS phase shift matrices are identical across both stages (i.e., $\boldsymbol{\Phi}_1 = \boldsymbol{\Phi}_2$), then the FIM $\boldsymbol{J}$ becomes singular, leading to an unbounded CRB, i.e., $\text{CRB}(\theta) = \infty$. Otherwise, $\boldsymbol{J}$ is invertible, ensuring a bounded $\text{CRB}(\theta)$.*

Proof. Recall that $\text{rank}(\boldsymbol{G}) = 1$, the channel can be written as $\boldsymbol{G} = \sigma\boldsymbol{p}\boldsymbol{q}^H$. From equations (74)–(76), the determinant of the FIM $\boldsymbol{J}$ can be expressed as (18) shown at the top of the next page. If $\boldsymbol{\Phi}_1 = \boldsymbol{\Phi}_2$, then we have $\mu_1 = \mu_2$ and $\tilde{\mu}_1 = \tilde{\mu}_2$. Consequently, the term $|\tilde{\mu}_1\mu_2^* - \tilde{\mu}_2\mu_1^*|^2$ in (18) becomes zero, implying that $\det(\boldsymbol{J}) = 0$. Hence, the FIM is singular and the CRB becomes unbounded. □

Remark 1. *This result shows that when the channel is rank-one, it is necessary to employ different IRS phase-shift configurations across the two sensing stages to ensure a bounded CRB. This insight is critical for the practical design of IRS reflective coefficients.*

IV. CRB Minimization via Joint Transmit Beamforming and IRS Optimization

In this section, we formulate and solve the joint transmit beamforming and IRS optimization problem in order to minimize the estimation CRB.

For a target with DOA θ, the CRB minimization problem is formulated as

$$\begin{aligned}(\text{P1}): \min_{\boldsymbol{w},\boldsymbol{\psi}_1,\boldsymbol{\psi}_2} \ & \text{CRB}(\theta) \\ \text{s.t.} \ \ & \|\boldsymbol{w}\|_2^2 \le P_T, && \text{(19a)} \\ & |[\boldsymbol{\psi}_i]_n| = 1, \forall i \in \{1,2\}, \forall n \in \{1,\cdots,N\}. && \text{(19b)}\end{aligned}$$

Note that in the CRB expression (16), there is no coupling between the IRS phase shifts and the transmit beamformer.

$$\mathrm{CRB}(\theta)=\frac{\sigma_N^2}{8T\sigma^4|\alpha|^2\pi^2\cos^2(\theta)\big(\mu_1\bar{\mu}_1+\mu_2\bar{\mu}_2-\frac{|\mu_1\tilde{\mu}_1+\mu_2\tilde{\mu}_2|^2}{|\mu_1|^2+|\mu_2|^2}\big)|\boldsymbol{q}^H\boldsymbol{w}|^2} \tag{16}$$

$$\begin{aligned}\det(\boldsymbol{J})=&\frac{8T^3|\alpha|^2}{\sigma_N^6}\left(\mathrm{tr}(\boldsymbol{Q}\boldsymbol{R}_x\boldsymbol{Q}^H)\mathrm{tr}(\dot{\boldsymbol{Q}}\boldsymbol{R}_x\dot{\boldsymbol{Q}}^H)-|\mathrm{tr}(\boldsymbol{Q}\boldsymbol{R}_x\dot{\boldsymbol{Q}}^H)|^2\right)\\=&\frac{32\sigma^8\pi^2\cos^2(\theta)T^3|\alpha|^2}{\sigma_N^6}\left((\mu_1\bar{\mu}_1+\mu_2\bar{\mu}_2)(|\mu_1|^2+|\mu_2|^2)-|\mu_1\tilde{\mu}_1+\mu_2\tilde{\mu}_2|^2\right)|\boldsymbol{q}^H\boldsymbol{w}|^4\\=&\frac{32\sigma^8\pi^2\cos^2(\theta)T^3|\alpha|^2}{\sigma_N^6}\left(|\tilde{\mu}_1\mu_2^*|^2+|\tilde{\mu}_2\mu_1^*|^2-2\Re\{\mu_1\tilde{\mu}_1\tilde{\mu}_2^*\mu_2^*\}\right)|\boldsymbol{q}^H\boldsymbol{w}|^4\\=&\frac{32\sigma^8\pi^2\cos^2(\theta)T^3|\alpha|^2}{\sigma_N^6}(|\tilde{\mu}_1\mu_2^*-\tilde{\mu}_2\mu_1^*|^2)|\boldsymbol{q}^H\boldsymbol{w}|^4\end{aligned} \tag{18}$$

This decoupling allows for the independent optimization of these two factors. Specifically, the objective function in (19) can be decomposed into two distinct components: one that depends solely on the IRS reflective coefficients and another that depends exclusively on the transmit beamformer. Consequently, the original optimization problem can be decoupled into two sub-problems, i.e., transmit beamformer optimization and IRS reflective coefficients optimization. In the following, we provide detailed formulations and solution approaches for these two sub-problems.

A. Transmit Beamforming: An Optimal Closed Form Design

First, we optimize the transmit beamformer $\boldsymbol{w}$ in problem $(\mathrm{P1})$ while keeping the reflective coefficients reflective coefficients $\boldsymbol{\psi}_1$ and $\boldsymbol{\psi}_2$ fixed. Given the CRB expression in (16), the optimization problem $(\mathrm{P1})$ can then be recast as

$$\begin{aligned}(\mathrm{P2}):\ \max_{\boldsymbol{w}}\quad&|\boldsymbol{q}^H\boldsymbol{w}|^2\\ \text{s.t.}\quad&\|\boldsymbol{w}\|_2^2\le P_T.\end{aligned} \tag{20}$$

Hence, the CRB-minimization-based transmit beamformer optimization problem simplifies to maximizing the radiation power in the direction of the IRS. Following a similar formulation as in [28], we demonstrate that problem (20) admits a closed-form optimal solution, i.e.,

$$\boldsymbol{w}=\sqrt{P_T}\boldsymbol{q}. \tag{21}$$

B. IRS Reflective Coefficients Optimization

Next, for a given transmit beamformer $\boldsymbol{w}$, we optimize the reflective beamformers $\boldsymbol{\psi}_1$ and $\boldsymbol{\psi}_2$ in problem (P1). In the CRB expression (16), only μ_i, $\bar{\mu}_i$ and $\tilde{\mu}_i$ are dependent on the IRS coefficients, where $i\in\{1,2\}$. To facilitate the derivation, we focus on the terms associated with the IRS. Under this setting, the reflective beamformer optimization problem can be formulated as

$$\begin{aligned}(\mathrm{P3}):\ \max_{\boldsymbol{\psi}_1,\boldsymbol{\psi}_2}\quad&\mu_1\bar{\mu}_1+\mu_2\bar{\mu}_2-\frac{|\mu_1\tilde{\mu}_1+\mu_2\tilde{\mu}_2|^2}{|\mu_1|^2+|\mu_2|^2}\\ \text{s.t.}\quad&\mu_i=\boldsymbol{\psi}_i^H\boldsymbol{F}\boldsymbol{\psi}_i, &\text{(22a)}\\&\bar{\mu}_i=\boldsymbol{\psi}_i^H\boldsymbol{D}\boldsymbol{F}\boldsymbol{D}\boldsymbol{\psi}_i, &\text{(22b)}\\&\tilde{\mu}_i=\boldsymbol{\psi}_i^H\boldsymbol{D}\boldsymbol{F}\boldsymbol{\psi}_i, &\text{(22c)}\\&|[\boldsymbol{\psi}_i]_n|=1,\forall i\in\{1,2\},\forall n\in\{1,\cdots,N\}. &\text{(22d)}\end{aligned}$$

Substituting (22a), (22b), and (22c) into the objective function of (22), the problem (P3) can be rewritten as

$$\begin{aligned}(\mathrm{P3.1}):\ \max_{\boldsymbol{\psi}_1,\boldsymbol{\psi}_2}\quad&f(\boldsymbol{\psi}_1,\boldsymbol{\psi}_2)\\ \text{s.t.}\quad&\text{(22d)},\end{aligned} \tag{23}$$

where $f(\boldsymbol{\psi}_1,\boldsymbol{\psi}_2)$ is calculated as

$$\begin{aligned}&f(\boldsymbol{\psi}_1,\boldsymbol{\psi}_2)\\=&\boldsymbol{\psi}_1^H\boldsymbol{F}\boldsymbol{\psi}_1\boldsymbol{\psi}_1^H\boldsymbol{D}\boldsymbol{F}\boldsymbol{D}\boldsymbol{\psi}_1+\boldsymbol{\psi}_2^H\boldsymbol{F}\boldsymbol{\psi}_2\boldsymbol{\psi}_2^H\boldsymbol{D}\boldsymbol{F}\boldsymbol{D}\boldsymbol{\psi}_2\\&-\frac{|\boldsymbol{\psi}_1^H\boldsymbol{F}\boldsymbol{\psi}_1\boldsymbol{\psi}_1^H\boldsymbol{D}\boldsymbol{F}\boldsymbol{\psi}_1+\boldsymbol{\psi}_2^H\boldsymbol{F}\boldsymbol{\psi}_2\boldsymbol{\psi}_2^H\boldsymbol{D}\boldsymbol{F}\boldsymbol{\psi}_2|^2}{|\boldsymbol{\psi}_1^H\boldsymbol{F}\boldsymbol{\psi}_1|^2+|\boldsymbol{\psi}_2^H\boldsymbol{F}\boldsymbol{\psi}_2|^2}.\end{aligned} \tag{24}$$

However, the problem $(\mathrm{P3.1})$ is non-convex due to the non-concavity of the objective function with respect to the IRS phase shifts, and the unit-modulus constraint. To address this challenge, we first handle the unit-modulus constraint and then employ the majorization-minimization (MM) method to solve the resulting non-convex optimization problem.

Define $\boldsymbol{V}_i=\boldsymbol{\psi}_i\boldsymbol{\psi}_i^H\in\mathbb{C}^{N\times N}$ with $\boldsymbol{V}_i\succeq\boldsymbol{0}$ and $\mathrm{rank}(\boldsymbol{V}_i)=1$. Based on (22d), $[\boldsymbol{V}_i]_{n,n}=1,\forall n\in\{1,2,\cdots,N\}$. We have $\mu_i=\boldsymbol{\psi}_i^H\boldsymbol{F}\boldsymbol{\psi}_i=\mathrm{tr}(\boldsymbol{F}\boldsymbol{V}_i)$, $\bar{\mu}_i=\boldsymbol{\psi}_i^H\boldsymbol{D}\boldsymbol{F}\boldsymbol{D}\boldsymbol{\psi}_i=\mathrm{tr}(\boldsymbol{D}\boldsymbol{F}\boldsymbol{D}\boldsymbol{V}_i)$ and $\tilde{\mu}_i=\boldsymbol{\psi}_i^H\boldsymbol{D}\boldsymbol{F}\boldsymbol{\psi}_i=\mathrm{tr}(\boldsymbol{D}\boldsymbol{F}\boldsymbol{V}_i),i\in\{1,2\}$. Therefore, by introducing $\boldsymbol{V}_i$ and relaxing the rank-one constraint, the optimization problem

(P3.1) can be equivalently reformulated as follows:

$$\begin{aligned}&(\mathrm{P4}):\\ \min_{\boldsymbol{V}_1,\boldsymbol{V}_2}\quad & f(\boldsymbol{V}_1,\boldsymbol{V}_2)\\ \text{s.t.}\quad & [\boldsymbol{V}_i]_{n,n}=1,\forall n\in\{1,2,\cdots,N\},i\in\{1,2\}, \quad (25a)\\ & \boldsymbol{V}_i\succeq\mathbf{0}, \quad (25b)\end{aligned}$$

where $f(\boldsymbol{V}_1,\boldsymbol{V}_2)$ can be expressed as

$$\begin{aligned}&f(\boldsymbol{V}_1,\boldsymbol{V}_2)\\ =&-\left(\mathrm{tr}(\boldsymbol{F}\boldsymbol{V}_1)\mathrm{tr}(\boldsymbol{D}\boldsymbol{F}\boldsymbol{D}\boldsymbol{V}_1)+\mathrm{tr}(\boldsymbol{F}\boldsymbol{V}_2)\mathrm{tr}(\boldsymbol{D}\boldsymbol{F}\boldsymbol{D}\boldsymbol{V}_2)\right)\\ &+\frac{|\mathrm{tr}(\boldsymbol{F}\boldsymbol{V}_1)\mathrm{tr}(\boldsymbol{D}\boldsymbol{F}\boldsymbol{V}_1)+\mathrm{tr}(\boldsymbol{F}\boldsymbol{V}_2)\mathrm{tr}(\boldsymbol{D}\boldsymbol{F}\boldsymbol{V}_2)|^2}{\mathrm{tr}^2(\boldsymbol{F}\boldsymbol{V}_1)+\mathrm{tr}^2(\boldsymbol{F}\boldsymbol{V}_2)}. \quad (26)\end{aligned}$$

Note that in (25), all constraints are convex, however, the objective function $f(\boldsymbol{V}_1,\boldsymbol{V}_2)$ is non-concave, rendering problem (P4) non-convex. To address this issue, we employ a MM framework, which is implemented iteratively to solve this problem. To this end, we first introduce the following theorem.

Theorem 1. *Let $f(\boldsymbol{x})$ be a continuously differentiable function with its domain defined as $\mathrm{dom}f$. Suppose its gradient $\nabla f(\boldsymbol{x})$ is Lipschitz continuous with constant $L>0$, i.e.,*

$$\|\nabla f(\boldsymbol{x})-\nabla f(\boldsymbol{y})\|_2\le L\|\boldsymbol{x}-\boldsymbol{y}\|_2, \quad (27)$$

for all $\boldsymbol{x},\boldsymbol{y}\in\mathrm{dom}f$. If $\mathrm{dom}f$ is convex, then for all $\boldsymbol{x},\boldsymbol{y}\in\mathrm{dom}f$, we have

$$f(\boldsymbol{y})\le f(\boldsymbol{x})+\nabla f(\boldsymbol{x})^T(\boldsymbol{y}-\boldsymbol{x})+\frac{L}{2}\|\boldsymbol{y}-\boldsymbol{x}\|_2^2. \quad (28)$$

Let f_{ub} denote the right-hand side of the inequality, i.e.,

$$f_{\mathrm{ub}}(\boldsymbol{x},\boldsymbol{y})\triangleq f(\boldsymbol{x})+\nabla f(\boldsymbol{x})^T(\boldsymbol{y}-\boldsymbol{x})+\frac{L}{2}\|\boldsymbol{y}-\boldsymbol{x}\|_2^2. \quad (29)$$

Then $f_{\mathrm{ub}}(\boldsymbol{x},\boldsymbol{y})$ serves as a quadratic upper bound for $f(\boldsymbol{y})$.

Proof. See Appendix B. □

Following the Theorem 1, we have the following proposition.

Proposition 2. *For the function $f(\boldsymbol{V}_1,\boldsymbol{V}_2)$ in (26), $\forall\boldsymbol{V}_i\in\mathrm{dom}\boldsymbol{V},i\in\{1,2\}$. For all $\boldsymbol{V}_{1,(t)},\boldsymbol{V}_{2,(t)}\in\mathrm{dom}\boldsymbol{V}$, we have*

$$f(\boldsymbol{V}_1,\boldsymbol{V}_2)\le f_{\mathrm{ub}}(\boldsymbol{V}_{1,(t)},\boldsymbol{V}_{2,(t)},\boldsymbol{V}_1,\boldsymbol{V}_2), \quad (30)$$

and

$$\begin{aligned}f_{\mathrm{ub}}(\boldsymbol{V}_{1,(t)},\boldsymbol{V}_{2,(t)},\boldsymbol{V}_1,\boldsymbol{V}_2)&=f(\boldsymbol{V}_{1,(t)},\boldsymbol{V}_{2,(t)})\\ &+\mathrm{tr}\left(\nabla f(\boldsymbol{V}_{1,(t)},\boldsymbol{V}_{2,(t)})^T\boldsymbol{R}\right)+\frac{L}{2}\|\boldsymbol{R}\|_F^2, \quad (31)\end{aligned}$$

where L is Lipschitz constant, $\nabla f(\boldsymbol{V}_{1,(t)},\boldsymbol{V}_{2,(t)})$ denotes the gradient of $f(\boldsymbol{V}_1,\boldsymbol{V}_2)$ at the point $(\boldsymbol{V}_{1,(t)},\boldsymbol{V}_{2,(t)})$, and

$$\boldsymbol{R}=\begin{bmatrix}\boldsymbol{V}_1-\boldsymbol{V}_{1,(t)}\\ \boldsymbol{V}_2-\boldsymbol{V}_{2,(t)}\end{bmatrix}\in\mathbb{C}^{2N\times N}. \quad (32)$$

The detailed derivations of the gradient of $f(\boldsymbol{V}_1,\boldsymbol{V}_2)$ are provided in Appendix C.

Proof. See Appendix D. □

Next, building on Proposition 2, we obtain a quadratic upper bound for the objective function in (25). Specifically, given the solutions of the t-th inner iteration, $\boldsymbol{V}_{1,(t)}$ and $\boldsymbol{V}_{2,(t)}$, we construct a more tractable surrogate function that approximates the objective function $f(\boldsymbol{V}_1,\boldsymbol{V}_2)$, i.e.,

$$f(\boldsymbol{V}_1,\boldsymbol{V}_2)\le f_{\mathrm{ub}}(\boldsymbol{V}_{1,(t)},\boldsymbol{V}_{2,(t)},\boldsymbol{V}_1,\boldsymbol{V}_2). \quad (33)$$

Notice that in the expression of the upper bound function (31), $f(\boldsymbol{V}_{1,(t)},\boldsymbol{V}_{2,(t)})$ is independent of $(\boldsymbol{V}_1,\boldsymbol{V}_2)$, making it a constant term. The term $\mathrm{tr}\left(\nabla f(\boldsymbol{V}_{1,(t)},\boldsymbol{V}_{2,(t)})^T\boldsymbol{R}\right)$ is linear in $(\boldsymbol{V}_1,\boldsymbol{V}_2)$ and, therefore, convex with respect to $(\boldsymbol{V}_1,\boldsymbol{V}_2)$. Furthermore, the Frobenius norm term

$$\frac{L}{2}\|\boldsymbol{R}\|_F^2=\frac{L}{2}\mathrm{tr}(\boldsymbol{R}^H\boldsymbol{R}) \quad (34)$$

is also convex with respect to $(\boldsymbol{V}_1,\boldsymbol{V}_2)$ for $L>0$. Consequently, the upper bound function $f_{\mathrm{ub}}(\boldsymbol{V}_{1,t},\boldsymbol{V}_{2,t},\boldsymbol{V}_1,\boldsymbol{V}_2)$ is convex. By replacing the objective function in (25) with $f_{\mathrm{ub}}(\boldsymbol{V}_{1,t},\boldsymbol{V}_{2,t},\boldsymbol{V}_1,\boldsymbol{V}_2)$, problem (25) can be approximated in the t-th inner iteration as the following convex form:

$$\begin{aligned}&(\mathrm{P4}.t):\\ \min_{\boldsymbol{V}_1,\boldsymbol{V}_2}\quad & f_{\mathrm{ub}}(\boldsymbol{V}_{1,(t)},\boldsymbol{V}_{2,(t)},\boldsymbol{V}_1,\boldsymbol{V}_2)\\ \text{s.t.}\quad & [\boldsymbol{V}_i]_{n,n}=1,\forall n\in\{1,2,\cdots,N\},i\in\{1,2\}, \quad (35a)\\ & \boldsymbol{V}_i\succeq\mathbf{0}, \quad (35b)\end{aligned}$$

which can be optimally solved using convex solvers such as CVX. Let $\hat{\boldsymbol{V}}_1^{(t)}$ and $\hat{\boldsymbol{V}}_2^{(t)}$ denote the optimal solutions of problem (P4.t), which are then updated to be the local points $\boldsymbol{V}_{1,(t+1)}$ and $\boldsymbol{V}_{2,(t+1)}$ for the next inner iteration. Since $f_{\mathrm{ub}}(\boldsymbol{V}_{1,(t)},\boldsymbol{V}_{2,(t)},\boldsymbol{V}_1,\boldsymbol{V}_2)$ serves an upper bound of $f(\boldsymbol{V}_1,\boldsymbol{V}_2)$, the inner iteration ensures that the objective value of problem (P4) will not increase i.e.,

$$f(\boldsymbol{V}_{1,(t+1)},\boldsymbol{V}_{2,(t+1)})\le f(\boldsymbol{V}_{1,(t)},\boldsymbol{V}_{2,(t)}). \quad (36)$$

Therefore, the convergence of MM algorithm for solving problem (P4) is ensured, and a suboptimal solution of problem (P4) is obtained. Let $\boldsymbol{V}_1^\star$ and $\boldsymbol{V}_2^\star$ denote the solutions to problem (P4) obtained via MM, where $\mathrm{rank}(\boldsymbol{V}_i^\star)>1$ may hold in general. Finally, based on $\boldsymbol{V}_1^\star$ and $\boldsymbol{V}_2^\star$, we construct approximate rank-one solutions for $\boldsymbol{V}_1$ and $\boldsymbol{V}_2$ for problem (P3) or (P4).

To recover $\boldsymbol{\psi}_i$ from $\boldsymbol{V}_i^\star$, a direct approach is to solve the following problem, i.e.,

$$\begin{aligned}\boldsymbol{\psi}_i^\star=\arg\min_{\boldsymbol{\psi}_i}\ &\|\boldsymbol{V}_i^\star-\boldsymbol{\psi}_i\boldsymbol{\psi}_i^H\|_F^2\\ \text{s.t.}\quad &(22d). \quad (37)\end{aligned}$$

A feasible solution to this problem can be obtained via eigenvalue decomposition (EVD). Specifically, if we decompose $\boldsymbol{V}_i^\star$ as $\boldsymbol{V}_i^\star=\sum_{p=1}^N\lambda_{i,p}\boldsymbol{v}_{i,p}\boldsymbol{v}_{i,p}^H$, where $\lambda_{i,1}\ge\lambda_{i,2}\ge\cdots\ge\lambda_{i,N}$ are the eigenvalues and $\boldsymbol{v}_{i,p}$ are the corresponding eigenvectors, a feasible solution after projection onto the constraint set of $\boldsymbol{\psi}_i$ is given by

$$\boldsymbol{\psi}_i^\star=\tilde{\boldsymbol{v}}_{i,1}, \quad (38)$$

where $\tilde{\boldsymbol{v}}_i\in\mathbb{C}^N$ is defined such that its nth element satisfies $[\tilde{\boldsymbol{v}}_i]_n\triangleq\frac{[\boldsymbol{v}_{i,1}]_n}{|[\boldsymbol{v}_{i,1}]_n|},i\in\{1,2\}$.

An alternative method to construct rank-one solutions is Gaussian randomization. In this approach, we independently generate random realizations $\boldsymbol{\nu}_i \sim \mathcal{CN}(\mathbf{0}, \boldsymbol{V}_i^\star)$, and construct a set of candidate feasible solutions as

$$\boldsymbol{\psi}_i = e^{j\arg(\boldsymbol{\nu}_i)}. \tag{39}$$

Then, the objective value of (P4) is approximated as the minimum one attained by the best $\boldsymbol{\psi}_i$, leading to suboptimal solutions $\boldsymbol{\psi}_i^\star, i \in \{1, 2\}$.

C. Computational Complexity Analysis

We analyze the computational complexity of the proposed CRB minimization-based method. Our proposed algorithm involves interatively solving the convex problem (P4.t). Since (P4.t) does not yield an analytical solution, the interior point method can be employed. The computational complexity of the interior point method at each iteration is in the order of

$$\mathcal{O}(d^3 + m^2 d + m d^2), \tag{40}$$

where d denotes the number of variables and m denotes the number of linear constraints. For our proposed method, there are $N(N+1)$ variables, and $2N$ linear constraints. Therefore, the computational complexity in each iteration is

$$\begin{aligned}\mathcal{O}\big((N(N+1))^3 + (2N)^2 \cdot N(N+1) \\ +2N \cdot (N(N+1))^2\big) = \mathcal{O}(N^6).\end{aligned} \tag{41}$$

Let ϵ denote the iteration accuracy. Thus, the overall computational complexity of solving (P4.t) is given by

$$\mathcal{O}\left(I\left((N^6)\cdot \log_2(\frac{1}{\epsilon})\right)\right), \tag{42}$$

where I denotes the number of iterations required for convergence.

D. Discussions: Illumination Diversity and Scaling Law

1) IRS Illumination diversity: Note that the proposed method primarily leverages the diversity of IRS illumination patterns across the two sensing stages. To characterize this IRS-induced diversity, we revisit equation (24), which is inversely proportional to the CRB for DOA estimation. Let us define $\boldsymbol{P} = \mathrm{diag}(\boldsymbol{p}) \in \mathbb{C}^{N\times N}$, so that $\boldsymbol{F} = \boldsymbol{P}^H \boldsymbol{a}^* \boldsymbol{a}^T \boldsymbol{P}$. Then, we have

$$\begin{aligned}\boldsymbol{\psi}_1^H \boldsymbol{F} \boldsymbol{\psi}_1 =& \boldsymbol{\psi}_1^H \boldsymbol{P}^H \boldsymbol{a}^* \boldsymbol{a}^T \boldsymbol{P} \boldsymbol{\psi}_1 \\ =& |\boldsymbol{a}^T \boldsymbol{P} \boldsymbol{\psi}_1|^2, \end{aligned} \tag{43a}$$

$$\begin{aligned}\boldsymbol{\psi}_1^H \boldsymbol{D}\boldsymbol{F} \boldsymbol{\psi}_1 =& \boldsymbol{\psi}_1^H \boldsymbol{D}\boldsymbol{P}^H \boldsymbol{a}^* \boldsymbol{a}^T \boldsymbol{P} \boldsymbol{\psi}_1 \\ =& \boldsymbol{a}^T \boldsymbol{P} \boldsymbol{\psi}_1 \boldsymbol{\psi}_1^H \boldsymbol{D}\boldsymbol{P}^H \boldsymbol{a}^*, \end{aligned} \tag{43b}$$

$$\begin{aligned}\boldsymbol{\psi}_1^H \boldsymbol{D}\boldsymbol{F}\boldsymbol{D} \boldsymbol{\psi}_1 =& \boldsymbol{\psi}_1^H \boldsymbol{D}\boldsymbol{P}^H \boldsymbol{a}^* \boldsymbol{a}^T \boldsymbol{P}\boldsymbol{D} \boldsymbol{\psi}_1 \\ =& |\boldsymbol{a}^T \boldsymbol{P}\boldsymbol{D} \boldsymbol{\psi}_1|^2, \end{aligned} \tag{43c}$$

Substituting (43) into (24), we obtain (44) shown at the top of the next page.

Specifically, the denominator of (44) satisfies

$$\frac{|\boldsymbol{a}^T \boldsymbol{P} \boldsymbol{\psi}_1|^2}{|\boldsymbol{a}^T \boldsymbol{P} \boldsymbol{\psi}_2|^2} + \frac{|\boldsymbol{a}^T \boldsymbol{P} \boldsymbol{\psi}_2|^2}{|\boldsymbol{a}^T \boldsymbol{P} \boldsymbol{\psi}_1|^2} \geq 2, \tag{45}$$

with the equality holds only if $|\boldsymbol{a}^T \boldsymbol{P} \boldsymbol{\psi}_1|^2 = |\boldsymbol{a}^T \boldsymbol{P} \boldsymbol{\psi}_2|^2$. We thus can define the numerator of (44) as a metric for quantifying IRS illumination diversity between the two stages:

$$\eta_\psi = |\boldsymbol{a}^T \boldsymbol{P} \boldsymbol{\psi}_1 \boldsymbol{a}^T \boldsymbol{P}\boldsymbol{D} \boldsymbol{\psi}_2 - \boldsymbol{a}^T \boldsymbol{P} \boldsymbol{\psi}_2 \boldsymbol{a}^T \boldsymbol{P}\boldsymbol{D} \boldsymbol{\psi}_1|^2. \tag{46}$$

Clearly, a larger value of η_ψ implies a greater difference in IRS phase configurations between the two stages, leading to improved parameter identifiability and thus a lower CRB.

2) Scaling Law of CRB: According to *proposition 1*, the inequality (45) becomes an equality when $\boldsymbol{a}^T \boldsymbol{P} \boldsymbol{\psi}_1 = (\boldsymbol{a}^T \boldsymbol{P} \boldsymbol{\psi}_2)^*$. Define $u_i = \boldsymbol{a}^T \boldsymbol{P} \boldsymbol{\psi}_i$, $v_i = \boldsymbol{a}^T \boldsymbol{P}\boldsymbol{D} \boldsymbol{\psi}_i$, when the equality holds, we have $u_1^* = u_2$, and we can re-express (44) as

$$\begin{aligned}(44) =& \frac{|u_1 v_1^* - (u_1 v_1^*)^*|^2}{2} \\ =& 2|\Im\{u_1 v_1^*\}|^2 \leq 2|u_1 v_1^*|^2 = 2|u_1|^2 |v_1|^2. \end{aligned} \tag{47}$$

Maximizing $|u_i|$, we align the IRS phase shifts such that $\boldsymbol{\psi}_i = e^{-j\arg(\boldsymbol{a}(\theta)+\boldsymbol{p})}$. Thus, the maximum value is

$$\max\{|u_i|\} = \boldsymbol{a}^T \boldsymbol{P} \boldsymbol{\psi}_i = N. \tag{48}$$

For v_i, noting that $\boldsymbol{D}$ is a real diagonal matrix, we obtain

$$\max\{|v_i|\} = \boldsymbol{a}^T \boldsymbol{P}\boldsymbol{D} \boldsymbol{\psi}_i = \sum_{n=1}^{N} (n-1) = \frac{N(N-1)}{2}. \tag{49}$$

Substituting these bounds into (47), we get

$$(44) \leq \frac{N^4 (N-1)^2}{2} \propto N^6. \tag{50}$$

Therefore, the CRB decreases as

$$\mathrm{CRB} \propto \frac{1}{N^6}. \tag{51}$$

On the other hand, the number of antennas M related term in (16) can be expressed as

$$|\boldsymbol{q}^H \boldsymbol{w}|^2 \leq P_T |\boldsymbol{q}^H \boldsymbol{q}|^2 = P_T M^2. \tag{52}$$

Thus, the CRB scales as

$$\mathrm{CRB} \propto \frac{1}{M^2}. \tag{53}$$

The CRB analysis reveals that the number of IRS reflecting elements, N, has a significantly greater impact on estimation accuracy than the number of antennas, M. Specifically, the CRB scales as N^{-6} and M^{-2}, indicating that increasing N yields a much stronger improvement in estimation performance. This is because the IRS not only enhances signal reflection and spatial resolution, but also participates in the entire sensing process more extensively than the radar antenna array. In particular, the IRS is involved in four stages: receiving the signal from the radar transmitter, transmitting the beamformed signal toward the target, receiving the echo from the target, and transmitting the target echo back to the radar receiver. In contrast, the radar antenna array is involved in only two stages, transmission and reception. As a result, the IRS effectively contributes an array gain in both transmitting and receiving at multiple points in the propagation path, further amplifying its impact on the overall sensing performance. Therefore, optimizing N is more effective for reducing the CRB in IRS-assisted NLOS sensing systems.

$$
\begin{aligned}
(24) =&|\boldsymbol{a}^T\boldsymbol{P}\boldsymbol{\psi}_1|^2\cdot|\boldsymbol{a}^T\boldsymbol{P}\boldsymbol{D}\boldsymbol{\psi}_1|^2+|\boldsymbol{a}^T\boldsymbol{P}\boldsymbol{\psi}_2|^2\cdot|\boldsymbol{a}^T\boldsymbol{P}\boldsymbol{D}\boldsymbol{\psi}_2|^2\\
&-\frac{\left||\boldsymbol{a}^T\boldsymbol{P}\boldsymbol{\psi}_1|^2\cdot\boldsymbol{a}^T\boldsymbol{P}\boldsymbol{\psi}_1\boldsymbol{\psi}_1^H\boldsymbol{D}\boldsymbol{P}^H\boldsymbol{a}^*+|\boldsymbol{a}^T\boldsymbol{P}\boldsymbol{\psi}_2|^2\cdot\boldsymbol{a}^T\boldsymbol{P}\boldsymbol{\psi}_2\boldsymbol{\psi}_2^H\boldsymbol{D}\boldsymbol{P}^H\boldsymbol{a}^*\right|^2}{|\boldsymbol{a}^T\boldsymbol{P}\boldsymbol{\psi}_1|^4+|\boldsymbol{a}^T\boldsymbol{P}\boldsymbol{\psi}_2|^4}\\
=&\frac{|\boldsymbol{a}^T\boldsymbol{P}\boldsymbol{\psi}_1|^6\cdot|\boldsymbol{a}^T\boldsymbol{P}\boldsymbol{D}\boldsymbol{\psi}_1|^2+|\boldsymbol{a}^T\boldsymbol{P}\boldsymbol{\psi}_1|^2\cdot|\boldsymbol{a}^T\boldsymbol{P}\boldsymbol{\psi}_2|^4\cdot|\boldsymbol{a}^T\boldsymbol{P}\boldsymbol{D}\boldsymbol{\psi}_1|^2}{|\boldsymbol{a}^T\boldsymbol{P}\boldsymbol{\psi}_1|^4+|\boldsymbol{a}^T\boldsymbol{P}\boldsymbol{\psi}_2|^4}\\
&+\frac{|\boldsymbol{a}^T\boldsymbol{P}\boldsymbol{\psi}_2|^6\cdot|\boldsymbol{a}^T\boldsymbol{P}\boldsymbol{D}\boldsymbol{\psi}_2|^2+|\boldsymbol{a}^T\boldsymbol{P}\boldsymbol{\psi}_2|^2\cdot|\boldsymbol{a}^T\boldsymbol{P}\boldsymbol{\psi}_1|^4\cdot|\boldsymbol{a}^T\boldsymbol{P}\boldsymbol{D}\boldsymbol{\psi}_2|^2}{|\boldsymbol{a}^T\boldsymbol{P}\boldsymbol{\psi}_1|^4+|\boldsymbol{a}^T\boldsymbol{P}\boldsymbol{\psi}_2|^4}\\
&-\frac{|\boldsymbol{a}^T\boldsymbol{P}\boldsymbol{\psi}_1|^6\cdot|\boldsymbol{a}^T\boldsymbol{P}\boldsymbol{D}\boldsymbol{\psi}_2|^2+|\boldsymbol{a}^T\boldsymbol{P}\boldsymbol{\psi}_2|^6\cdot|\boldsymbol{a}^T\boldsymbol{P}\boldsymbol{D}\boldsymbol{\psi}_1|^2}{|\boldsymbol{a}^T\boldsymbol{P}\boldsymbol{\psi}_1|^4+|\boldsymbol{a}^T\boldsymbol{P}\boldsymbol{\psi}_2|^4}\\
&-\frac{2\cdot|\boldsymbol{a}^T\boldsymbol{P}\boldsymbol{\psi}_1|^2\cdot|\boldsymbol{a}^T\boldsymbol{P}\boldsymbol{\psi}_2|^2\cdot\Re\{\boldsymbol{a}^T\boldsymbol{P}\boldsymbol{\psi}_1(\boldsymbol{a}^T\boldsymbol{P}\boldsymbol{\psi}_2)^*(\boldsymbol{a}^T\boldsymbol{P}\boldsymbol{D}\boldsymbol{\psi}_1)^*(\boldsymbol{a}^T\boldsymbol{P}\boldsymbol{\psi}_2)\}}{|\boldsymbol{a}^T\boldsymbol{P}\boldsymbol{\psi}_1|^4+|\boldsymbol{a}^T\boldsymbol{P}\boldsymbol{\psi}_2|^4}\\
=&\frac{\left(|\boldsymbol{a}^T\boldsymbol{P}\boldsymbol{\psi}_1|^2|\boldsymbol{a}^T\boldsymbol{P}\boldsymbol{D}\boldsymbol{\psi}_2|^2+|\boldsymbol{a}^T\boldsymbol{P}\boldsymbol{\psi}_2|^2|\boldsymbol{a}^T\boldsymbol{P}\boldsymbol{D}\boldsymbol{\psi}_1|^2-2\Re\{\boldsymbol{a}^T\boldsymbol{P}\boldsymbol{\psi}_1(\boldsymbol{a}^T\boldsymbol{P}\boldsymbol{\psi}_2)^*(\boldsymbol{a}^T\boldsymbol{P}\boldsymbol{D}\boldsymbol{\psi}_1)^*(\boldsymbol{a}^T\boldsymbol{P}\boldsymbol{\psi}_2)\}\right)}{\frac{|\boldsymbol{a}^T\boldsymbol{P}\boldsymbol{\psi}_1|^2}{|\boldsymbol{a}^T\boldsymbol{P}\boldsymbol{\psi}_2|^2}+\frac{|\boldsymbol{a}^T\boldsymbol{P}\boldsymbol{\psi}_2|^2}{|\boldsymbol{a}^T\boldsymbol{P}\boldsymbol{\psi}_1|^2}}\\
=&\frac{|\boldsymbol{a}^T\boldsymbol{P}\boldsymbol{\psi}_1\boldsymbol{a}^T\boldsymbol{P}\boldsymbol{D}\boldsymbol{\psi}_2-\boldsymbol{a}^T\boldsymbol{P}\boldsymbol{\psi}_2\boldsymbol{a}^T\boldsymbol{P}\boldsymbol{D}\boldsymbol{\psi}_1|^2}{\frac{|\boldsymbol{a}^T\boldsymbol{P}\boldsymbol{\psi}_1|^2}{|\boldsymbol{a}^T\boldsymbol{P}\boldsymbol{\psi}_2|^2}+\frac{|\boldsymbol{a}^T\boldsymbol{P}\boldsymbol{\psi}_2|^2}{|\boldsymbol{a}^T\boldsymbol{P}\boldsymbol{\psi}_1|^2}}
\end{aligned}
\tag{44}
$$

V. The Maximum Likelihood Estimation

In this section, we derive the maximum likelihood estimation (MLE) method to estimate the target's direction of arrival (DOA) θ, we are interested in the mean squared error (MSE) performance of the MLE.

Based on (9), the vectorized received signal at the AP can be rewritten as

$$
\begin{aligned}
\tilde{\boldsymbol{y}}&=\alpha\mathrm{vec}(\boldsymbol{Q}\boldsymbol{X})+\boldsymbol{n}\\
&=\alpha\tilde{\boldsymbol{q}}(\theta)+\boldsymbol{n},
\end{aligned}
\tag{54}
$$

where $\tilde{\boldsymbol{q}}(\theta)=\mathrm{vec}(\boldsymbol{Q}\boldsymbol{X})$. The Likelihood fucntion of $\tilde{\boldsymbol{y}}$ given $\boldsymbol{\zeta}$ is

$$
f_{\tilde{\boldsymbol{y}}}(\tilde{\boldsymbol{y}};\boldsymbol{\zeta})=\frac{1}{(\pi\sigma_N^2)^{MT}}\exp\left(-\frac{1}{\sigma_N^2}\|\tilde{\boldsymbol{y}}-\alpha\tilde{\boldsymbol{q}}(\theta)\|_2^2\right).
\tag{55}
$$

In this case, maximizing $f_{\tilde{\boldsymbol{y}}}(\tilde{\boldsymbol{y}};\boldsymbol{\zeta})$ is equivalent to minimizing $\|\tilde{\boldsymbol{y}}-\alpha\tilde{\boldsymbol{q}}(\theta)\|_2^2$. Therefore, the MLE of θ and α is given by

$$
(\theta_{\mathrm{MLE}},\alpha_{\mathrm{MLE}})=\arg\min_{\theta,\alpha}\|\tilde{\boldsymbol{y}}-\alpha\tilde{\boldsymbol{q}}(\theta)\|_2^2.
\tag{56}
$$

Consequently, under any given θ, the MLE of α is attained as

$$
\alpha_{\mathrm{MLE}}=(\tilde{\boldsymbol{q}}^H(\theta)\tilde{\boldsymbol{q}}(\theta))^{-1}\tilde{\boldsymbol{q}}^H(\theta)\tilde{\boldsymbol{y}}.
\tag{57}
$$

Bringing (57) to (56), we have

$$
\begin{aligned}
&\|\tilde{\boldsymbol{y}}-\alpha\tilde{\boldsymbol{q}}(\theta)\|_2^2\\
&=\|\tilde{\boldsymbol{y}}\|_2^2-\frac{|\tilde{\boldsymbol{q}}^H(\theta)\tilde{\boldsymbol{y}}|^2}{\|\tilde{\boldsymbol{q}}(\theta)\|_2^2}\\
&=\|\tilde{\boldsymbol{y}}\|_2^2-\frac{|\mathrm{vec}(\boldsymbol{Q}\boldsymbol{X})^H\mathrm{vec}(\boldsymbol{Y})|^2}{\mathrm{vec}(\boldsymbol{Q}\boldsymbol{X})^H\mathrm{vec}(\boldsymbol{Q}\boldsymbol{X})}\\
&=\|\tilde{\boldsymbol{y}}\|_2^2-\frac{|\boldsymbol{Y}^{\mathrm{H}}\boldsymbol{Q}\boldsymbol{X}|^2}{\mathrm{tr}((\boldsymbol{Q}\boldsymbol{X})^H\boldsymbol{Q}\boldsymbol{X})}\\
&=\|\tilde{\boldsymbol{y}}\|_2^2-\frac{|\boldsymbol{C}^{\mathrm{T}}\boldsymbol{X}\boldsymbol{Y}^{\mathrm{H}}\boldsymbol{B}|^2}{T\mathrm{tr}(\boldsymbol{Q}\boldsymbol{R}_x\boldsymbol{Q}^H)}\\
&\overset{(a)}{=}\|\tilde{\boldsymbol{y}}\|_2^2-\frac{|\boldsymbol{b}_1^T\tilde{\boldsymbol{X}}\boldsymbol{Y}_{\boldsymbol{1}}^{\boldsymbol{H}}\boldsymbol{b}_{\boldsymbol{1}}+\boldsymbol{b}_2^T\tilde{\boldsymbol{X}}\boldsymbol{Y}_{\boldsymbol{2}}^{\boldsymbol{H}}\boldsymbol{b}_{\boldsymbol{2}}|^{\boldsymbol{2}}}{T(\boldsymbol{b}_1^T\boldsymbol{R}_{\tilde{\boldsymbol{x}}}\boldsymbol{b}_1^*\|\boldsymbol{b}_1\|_2^2+\boldsymbol{b}_2^T\boldsymbol{R}_{\tilde{\boldsymbol{x}}}\boldsymbol{b}_2^*\|\boldsymbol{b}_2\|_2^2)},
\end{aligned}
\tag{58}
$$

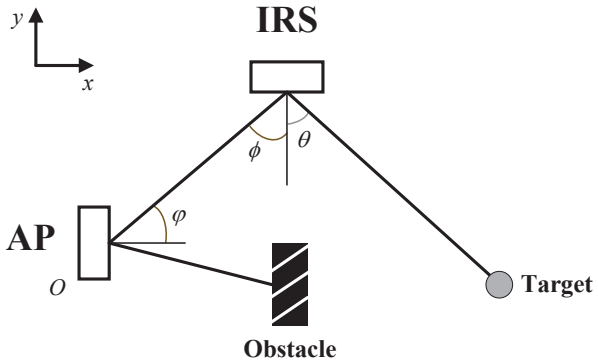

Fig. 2: Simulation setup (top view).

where (a) comes from that $\boldsymbol{Q}=\boldsymbol{B}\boldsymbol{C}^T=\mathrm{blkdiag}(\boldsymbol{b}_1\boldsymbol{b}_1^T,\boldsymbol{b}_2\boldsymbol{b}_2^T)$, $\boldsymbol{X}=\mathrm{blkdiag}(\tilde{\boldsymbol{X}},\tilde{\boldsymbol{X}})$, $\boldsymbol{Y}=[\boldsymbol{Y}_1\ \boldsymbol{Y}_2]$ and $\boldsymbol{Q}\boldsymbol{R}_x\boldsymbol{Q}^H=\mathrm{blkdiag}(\boldsymbol{b}_1^T\boldsymbol{R}_{\tilde{\boldsymbol{X}}}\boldsymbol{b}_1^*\boldsymbol{b}_1^H\boldsymbol{b}_1,\boldsymbol{b}_2^T\boldsymbol{R}_{\tilde{\boldsymbol{X}}}\boldsymbol{b}_2^*\boldsymbol{b}_2^H\boldsymbol{b}_2)$. Accordingly, the MLE of θ can be obtained by maximizing the second part in (58), i.e.,

$$
\theta_{\mathrm{MLE}}=\arg\max_{\theta}\frac{|\boldsymbol{b}_1^T\tilde{\boldsymbol{X}}\boldsymbol{Y}_{\boldsymbol{1}}^{\boldsymbol{H}}\boldsymbol{b}_{\boldsymbol{1}}+\boldsymbol{b}_2^T\tilde{\boldsymbol{X}}\boldsymbol{Y}_{\boldsymbol{2}}^{\boldsymbol{H}}\boldsymbol{b}_{\boldsymbol{2}}|^{\boldsymbol{2}}}{T(\boldsymbol{b}_1^T\boldsymbol{R}_{\tilde{\boldsymbol{x}}}\boldsymbol{b}_1^*\|\boldsymbol{b}_1\|_2^2+\boldsymbol{b}_2^T\boldsymbol{R}_{\tilde{\boldsymbol{x}}}\boldsymbol{b}_2^*\|\boldsymbol{b}_2\|_2^2)},
\tag{59}
$$

which can be easily solved via a one-dimensional search.

VI. Simulation Results

This section presents numerical results to assess the performance of the proposed IRS beamforming and transmit beamformer design based on CRB minimization. We consider a two-dimensional scenario, as depicted in Fig.2. The AP and IRS are positioned at coordinates $\boldsymbol{p}_{\mathrm{AP}}=[0,0]^T\mathrm{m}$ and $\boldsymbol{p}_{\mathrm{IRS}}=[4,4]^T\mathrm{m}$, respectively. In the simulations, the spacing d between adjacent antenna elements is set to half the signal wavelength. The AP-IRS channel is modeled using a geometric channel model, assuming only a LOS path, expressed as:

$$
\boldsymbol{G}=\varrho\boldsymbol{a}_{\mathrm{IRS}}(\phi)\boldsymbol{a}_{\mathrm{AP}}^H(\varphi),
\tag{60}
$$

This article has been accepted for publication in IEEE Transactions on Signal Processing. This is the author's version which has not been fully edited and content may change prior to final publication. Citation information: DOI 10.1109/TSP.2025.3609719

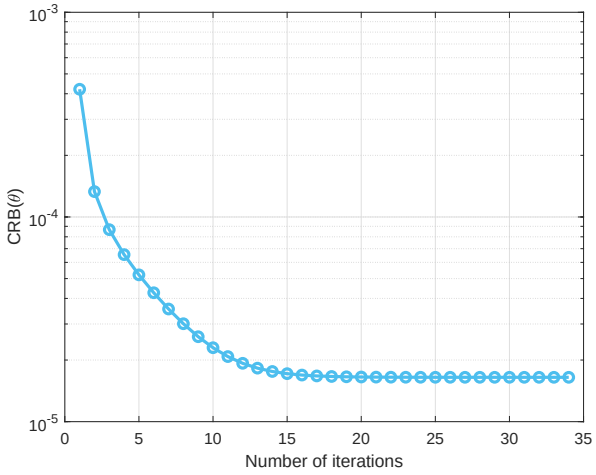

Fig. 3: Convergence behavior of the optimization problem, where SNR $= 0$dB, $M = N = 8$.

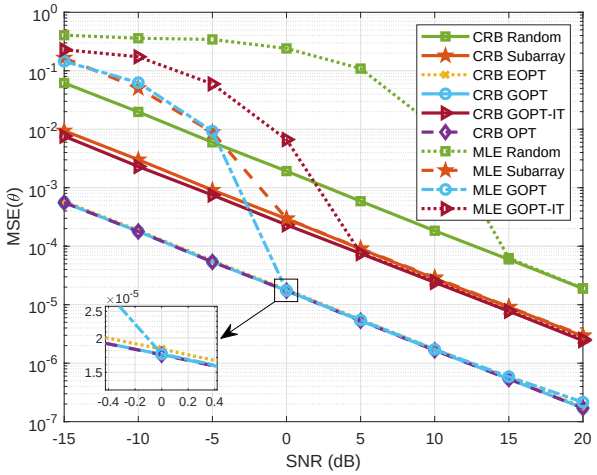

Fig. 4: MSEs and CRBs versus SNR.

where ϱ denotes the path loss between the AP and the IRS, and ϕ and φ denote the angle of arrival (AOA) and angle of departure (AOD), respectively. The path loss ϱ follows a distance-dependent model, $\mathcal{CN}(0, 10^{-0.1\kappa})$, where $\kappa = a + 10b\log_{10}(D) + \xi$. Here, $\xi \sim \mathcal{N}(0, \sigma_\xi^2)$, and D is the distance between the AP and the IRS. The parameters a, b, and σ_ξ are set to $a = 68$, $b = 2$, and $\sigma_\xi = 5.8$ dB, as recommended in [29], [30]. In the experiments, we consider one static target located within the angular range of $[30°, 40°]$ relative to the IRS, with its position at $\boldsymbol{p}_{\rm t} = [9, 0.5]^T$m. The direct link between the AP and the target is obstructed by obstacles, necessitating target detection via the IRS-assisted reflected path. For simplicity, the radar cross-section (RCS) of the target is set to 1 [20]. Then, the parameter α only accounts for the round-trip path loss of AP-IRS link, which is generated in a similar way as ϱ in (60).

Unless otherwise stated, the numbers of the AP's antennas and IRS's elements, as well as the transmit power, are set to $M = 8$, $N = 8$, and $P_T = 30$dBm, respectively. The received signal-to-noise ratio (SNR) is defined as

$$\text{SNR} \triangleq \frac{\|\boldsymbol{Y} - \boldsymbol{N}\|_F^2}{\|\boldsymbol{N}\|_F^2}, \tag{61}$$

where $\boldsymbol{Y}$ and $\boldsymbol{N}$ indicate the received signal and the additive noise in (8), respectively. All results are averaged over 10^3 Monte Carlo runs.

A. Performance Evaluation of the Proposed Method

The convergence behavior of the proposed method for solving problem (P4) is evaluated under the condition of SNR $= 0$dB, and $M = N = 8$. It is observed that the proposed alternating optimization-based algorithm converges within approximately 25 iterations, demonstrating its effectiveness and computational efficiency.

To examine the performance of our proposed method, we also employ the MLE method to estimate the target's DOA θ, and accordingly evaluate the MSE as the performance metric, which is define as

$$\text{MSE} = \mathbb{E}(\|\theta - \hat{\theta}\|_2^2), \tag{62}$$

where $\hat{\theta}$ denotes an estimate of the parameter θ. For our proposed CRB minimization method, the CRB result calculated directly using the optimal value of the convex relaxation (P4) is labeled as "OPT CRB". The CRB and MSE results attained by rank-one solutions approximated by EVD and Gaussian randomization are respectively labeled as "EOPT" and "GOPT". To illustrate the performance superiority of the proposed joint transmit beamforming and IRS optimization method, we also consider the following benchmark schemes.

1) Random Phase Shifts with Optimal Transmit Beamforming (labeled as "Random"): We consider the random IRS phase shifts, where the IRS phase shifts in both stages are independently drawn from a uniform distribution over $[0, 2\pi]$. Meanwhile, the transmit beamformer is optimized according to (20).

2) Subarray Partition based Phase Shifts Design with Optimal Transmit Beamforming (labeled as "Subarray"): This scheme was introduced in [19]. The entire IRS array is partitioned into multiple subarrays, each configured to generate a directional beam toward a specific direction. In following experiments, the IRS is divided into two subarrays, with beam directions set to $\{34°, 39°\}$ in phase 1 and $\{38°, 32°\}$ in phase 2. This configuration enables the IRS to generate directional beams for effective illumination of the potential target area while ensuring diverse illumination patterns across the two stages.

3) GOPT-based Phase Shifts with Isotropic Transmission (labeled as "GOPT-IT"): The IRS phase shifts are optmized to minimize CRB(θ) in (22) by solving problem (P3), where the Gaussian randomization method is employed to derive rank-one solutions. The AP utilizes isotropic transmission by employing a stochastic transmit beamformer, which is configured as $\boldsymbol{w} \sim \mathcal{CN}(0, \frac{P_T}{M}\boldsymbol{I}_M)$, ensuring uniform power allocation across all antennas.

This article has been accepted for publication in IEEE Transactions on Signal Processing. This is the author's version which has not been fully edited and content may change prior to final publication. Citation information: DOI 10.1109/TSP.2025.3609719

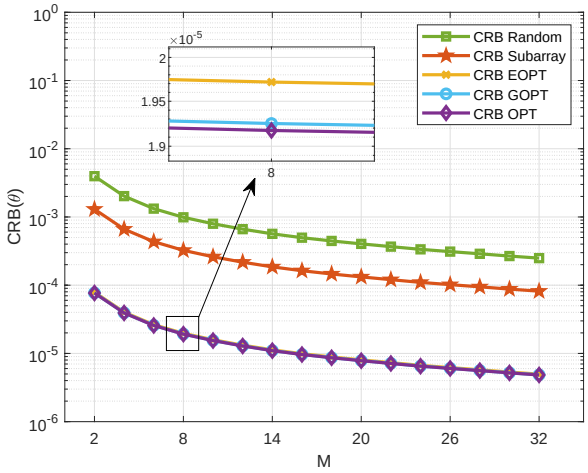

Fig. 5: CRBs versus the number of AP's antennas.

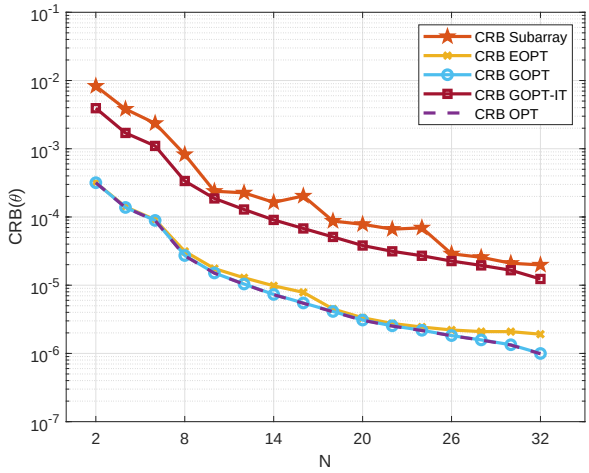

Fig. 6: CRBs versus the numbers of IRS's elements.

The CRB and MSE performance of the proposed method, along with other benchmark schemes, are illustrated in Fig.4 as a function of SNR. As shown in the figure, the CRB decreases monotonically and approximately linearly with increasing SNR. The proposed method (OPT) achieves the lowest CRB among all benchmark schemes. The feasible solutions obtained via eigenvalue decomposition and Gaussian randomization, denoted as EOPT and GOPT, respectively, closely approach the optimal CRB. However, the EOPT exhibits a slight performance degradation compared to GOPT. Notably, the MSE of GOPT remains close to its corresponding CRB even in relatively low SNR regimes, e.g. $\mathrm{SNR} = 0$dB, demonstrating the effectiveness of the proposed method. Moreover, due to the stochastic nature of the IRS phase shifts in the Random benchmark scheme, and the isotropic transmit beamformer in the GOPT-IT benchmark scheme, both schemes exhibit performance degradation compared to the proposed method.

Interestingly, in very low SNR regimes, such as $\mathrm{SNR} = -10$dB, the Subarray-based method achieves a lower MSE compared to the proposed scheme. This behavior can be attributed to two key factors. First, in such scenarios, the optimized CRB (CRB GOPT) cannot be achieved using maximum likelihood estimation (MLE), as the performance of MLE is highly sensitive to the power of the echo signals. Second, the Subarray-based IRS phase shift design generates a coarser beam pattern directed toward the potential angular range, which enhances robustness to noise. This results in a higher effective SNR, thereby improving its MLE performance. These findings align with the results reported in [20], where the SNR maximization scheme demonstrated superior MSE performance compared to the CRB optimization scheme under low transmit power conditions.

Additionally, In this simulation, the computed diversity metrics η_ψ defined in (46) for the schemes " GOPT", "EOPT", "Subarray", and "Random" are 4.7, 4.5, 0.28, and 0.26, respectively. These results further validate the effectiveness of the proposed method in enhancing IRS illumination diversity and improving estimation performance.

Next, we evaluate the CRB performance as a function of the number of AP antennas, as illustrated in Fig.5. In this experiment, the number of IRS reflecting elements is fixed at $N = 8$, and the SNR is set to 0dB. As anticipated, the CRB improves monotonically with an increasing number of antennas M. The proposed CRB minimization scheme achieves the best CRB performance across different choices of M. Specifically, the Gaussian randomization-based solution (GOPT) closely approaches the optimal CRB (OPT), while the eigenvalue decomposition-based solution (EOPT) exhibits a slight performance degradation.

In Fig.6, we present the CRB performance of the proposed method as a function of the number of IRS reflecting elements. In this experiment, the number of AP antennas is fixed at $M = 8$, and the SNR is set to 0dB. As expected, the CRB performance improves as the number of IRS elements N increases. The CRB achieved by both the Gaussian randomization-based solution (GOPT) and the EVD-based solution (EOPT) closely approaches that of the optimal solution (OPT).

It is also observed that the performance curve of GOPT-IT exhibits a constant offset relative to that of GOPT. This phenomenon can be attributed to the structure of the CRB expression in (16), where the IRS coefficients and the transmit beamformer contribute independently to the CRB. Since GOPT-IT employs the same IRS design as GOPT, the performance gap between their respective CRB values is primarily governed by the term $|\boldsymbol{q}^H\boldsymbol{w}|^2$.

B. Performance Comparison versus Different Levels of Rician Fading

Furthermore, to gain deeper insight, we evaluate the performance of the proposed method with respect to the rank of the AP-IRS channel matrix $\boldsymbol{G}$. To this end, the AP-IRS channel is modeled as Rician fading, expressed as:

$$\boldsymbol{G} = \sqrt{\frac{\gamma}{1+\gamma}}\boldsymbol{G}^{\mathrm{LOS}} + \sqrt{\frac{1}{1+\gamma}}\boldsymbol{G}^{\mathrm{NLOS}}, \tag{63}$$

where γ is the Rician factor (in dB), and $\boldsymbol{G}^{\mathrm{LOS}}$ and $\boldsymbol{G}^{\mathrm{NLOS}}$ denote the LOS and NLOS components, respectively. A typical

This article has been accepted for publication in IEEE Transactions on Signal Processing. This is the author's version which has not been fully edited and content may change prior to final publication. Citation information: DOI 10.1109/TSP.2025.3609719

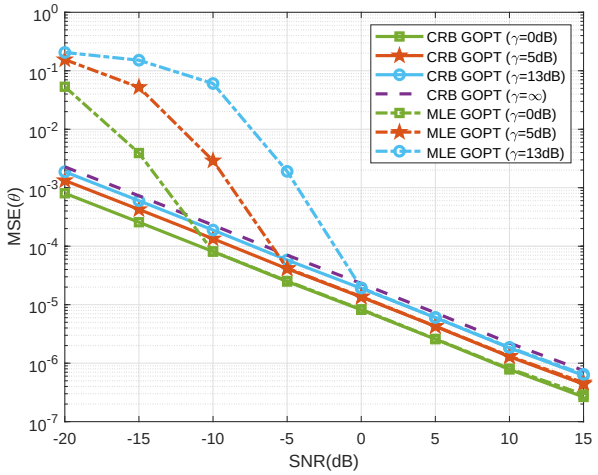

Fig. 7: MSEs and CRBs versus SNR under different levels of Rician fading, where $\mathrm{rank}(\boldsymbol{G}) = 2$.

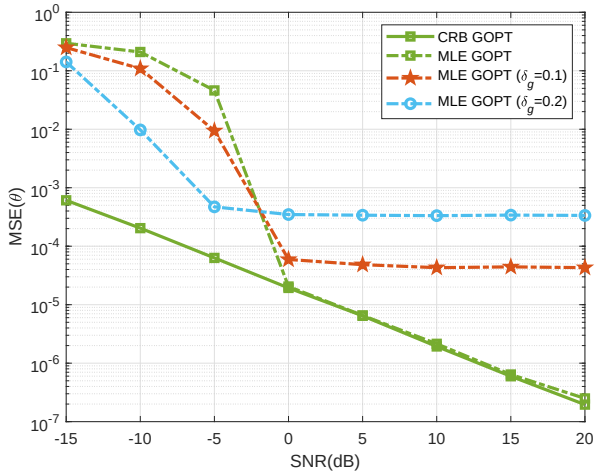

Fig. 8: MSEs and CRBs versus SNR under different levels of levels of channel uncertainty.

value of the Rician factor millimeter-wave (mmWave) band is 13dB [31]–[33], indicating that $\boldsymbol{G}$ is approximately a rank-one matrix. In our experiments, we assume one LOS path and one NLOS path between the AP and the IRS, leading to $\mathrm{rank}(\boldsymbol{G}) = 2$. To comprehensively examine the performance of the proposed method under diverse channel conditions, we also consider cases where the Rician factor is set to 0 dB and 5 dB. It is noteworthy that we directly apply our proposed method to the case where $\mathrm{rank}(\boldsymbol{G}) = 2$, even though it is originally derived for a rank-one AP-IRS channel. Specifically, for a rank-R AP-IRS channel matrix $\boldsymbol{G}$, we decompose it as $\boldsymbol{G} = \sum_{i=1}^{R} \sigma_i \boldsymbol{u}_i \boldsymbol{v}_i^H$, where $\sigma_1 \geq \sigma_2 \geq \cdots \geq \sigma_R$ are the singular values, and $\boldsymbol{u}_i$, $\boldsymbol{v}_i$ are the corresponding singular vectors. To ensure compatibility with our method, we construct a rank-one approximation $\tilde{\boldsymbol{G}} = \sigma_1 \boldsymbol{u}_1 \boldsymbol{v}_1^H$, under which the proposed approach can be directly applied.

Fig.7 presents the MSE and CRB results of the estimated DOA parameter as a function of SNR for different Rician factors. As observed, the MLE curves under various Rician factors closely achieve their respective CRBs in high SNR regime. Notably, the MLE performance for $\gamma = 13$dB closely matches that of the case where $\mathrm{rank}(\boldsymbol{G}) = 1$, i.e., $\gamma = \infty$, which is expected since the channel is dominated by the LOS component. Additionally, Fig.7 shows that both the CRB and the corresponding MLE performance improve as the Rician factor decreases. This result can be explained as follows. As the Rician factor decreases, the NLOS component of the channel matrix becomes stronger, providing additional diversity and making the parameters more distinguishable. This result demonstrates that the proposed method is not limited to rank-one channel matrices but is also effective in scenarios where the AP-IRS channel has a higher rank.

C. Imperfect AP-IRS Channel Condition

To comprehensively evaluate the performance of the proposed method, we consider the scenario where only imperfect knowledge of the AP-IRS channel $\boldsymbol{G}$ is available. Specifically, we adopt the statistical CSI error model [34], [35] to characterize the channel inaccuracies:

$$\boldsymbol{G} = \hat{\boldsymbol{G}} + \Delta \boldsymbol{G}, \tag{64}$$

where $\hat{\boldsymbol{G}}$ represents the estimated AP-IRS channel, and $\Delta \boldsymbol{G}$ denotes the channel estimation error. The entries of $\Delta \boldsymbol{G}$ follow a circularly symmetric complex Gaussian (CSCG) distribution, expressed as:

$$\mathrm{vec}(\Delta \boldsymbol{G}) \sim \mathcal{CN}(\boldsymbol{0}, \boldsymbol{\Sigma}_g),\ \boldsymbol{\Sigma}_g \succeq \boldsymbol{0}. \tag{65}$$

Here, $\boldsymbol{\Sigma}_g = \varepsilon_g^2 \boldsymbol{I}_{MN} \in \mathbb{C}^{MN \times MN}$ is the covariance matrix of the estimation error. In our experiments, the variance of $\mathrm{vec}(\Delta \boldsymbol{G})$ is defined as $\varepsilon_g^2 = \delta_g^2 \|\mathrm{vec}(\hat{\boldsymbol{G}})\|_2^2$, where $\delta_g \in [0, 1)$ quantifies the level of CSI uncertainty [34]. The CRB and MSE performance of the proposed method (GOPT) versus SNR under varying levels of channel uncertainty are illustrated in Fig.8. It is observed that the proposed method demonstrates robust performance even under imperfect CSI conditions for the AP-IRS channel. Specifically, at high SNR regimes, the MSE performance improves as the channel uncertainty decreases. Conversely, in low SNR regimes, higher channel uncertainty leads to better MSE performance. This intriguing phenomenon can be explained as follows. As channel uncertainty increases, the AP-IRS channel shifts from a rank-one matrix to a non-rank-one matrix. In such cases, the NLOS components of the channel matrix $\boldsymbol{G}$ introduce additional diversity, enhancing the ability to distinguish parameters. This diversity improves robustness to noise, resulting in better MSE performance.

D. Performance Evaluation with Discrete Phase Shifts

To further bridge the gap between ideal and practical implementations, we have also considered projecting the optimized continuous-phase solution onto discrete phase sets. Specifically, the set of discrete values of the phase shift coefficients is defined as

$$\psi_{i,n} \in \mathcal{F} \triangleq \left\{ 0, \frac{2\pi}{2^b}, \cdots, \frac{2\pi(2^b - 1)}{2^b} \right\}, \tag{66}$$

This article has been accepted for publication in IEEE Transactions on Signal Processing. This is the author's version which has not been fully edited and content may change prior to final publication. Citation information: DOI 10.1109/TSP.2025.3609719

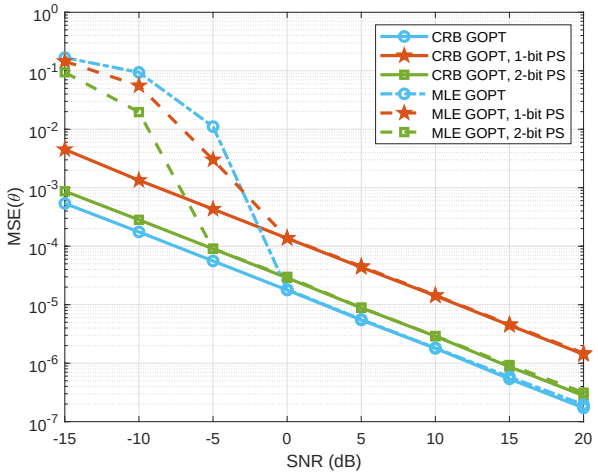

Fig. 9: MSEs and CRBs versus SNR.

where b denotes the resolution of the phase shifter. To meet the finite resolution constraint imposed on the phase shifters, a simple yet effective solution is to let each phase shift, $\psi_{i,n}$, take on a discrete value that is closest to its optimal (or near-optimal) value $\psi_{i,n}^{\star}$, i.e.,

$$\psi_{i,n}^{*} = \arg\min_{\psi\in\mathcal{F}} |\psi - \psi_{i,n}^{\star}|, \tag{67}$$

where $\psi_{i,n}^{\star}$ denotes the nth element of $\boldsymbol{\psi}_i^{\star}$. Fig.9 depicts the MSE and CRB results of our proposed solutions with both continuous-valued and discrete-valued IRS phase shifts. We see that 2-bit resolution can achieve a CRB that is close to that achieved with an infinite precision. Moreover, it is noteworthy that the MLE performence with discrete IRS phase shifts even surpasses that of the continuous solution in the low SNR regime. This is because discrete phase shifts yield broader beam patterns and suppress overfitting to noise, improving robustness at low SNR.

VII. Conclusion

This paper proposed an IRS-assisted NLOS wireless sensing system, where an IRS was employed to help an AP estimate parameters of a target in its NLOS region. To address the inherent scaling ambiguity in IRS-assisted sensing, a two-stage sensing scheme was introduced, and a succinct CRB expression for DOA estimation was derived, which decoupled the optimization of the transmit beamformer and IRS phase shifts. Leveraging this formulation, the optimal beamformer was obtained in closed form, while a majorization-minimization (MM)-based algorithm was employed to optimize the IRS reflective coefficients. Simulation results demonstrated that the proposed method achieved the lowest CRB and MSE among benchmark schemes, particularly in challenging scenarios where the degrees-of-freedom provided by the AP-IRS channel were insufficient to resolve the scaling ambiguity.

Several interesting issues remain open and merit further investigation. In multi-target scenarios, if the targets are well separated in both the angular and range domains, the surveillance area can be divided into resolution cells defined by distinct angle and range values. The proposed method can then be applied sequentially to each cell. However, when multiple targets are located within the same resolution cell, meaning they have similar directions and ranges, they become indistinguishable and are effectively treated as a single composite target. This limitation is inherent to conventional phased-array systems that employ directional beamforming with a single waveform. To address the challenge of closely spaced targets, one potential solution is to employ MIMO radar architectures that transmit orthogonal waveforms. This approach enables joint parameter estimation without relying on narrow beams. However, it typically comes at the cost of reduced beamforming gain, which is especially important in millimeter-wave systems. A detailed comparison between phased-array and MIMO radar architectures is beyond the scope of this work but represents a promising direction for future research.

Appendix A
Proof of Lemma2

Proof. Note that

$$\boldsymbol{B} = \boldsymbol{G}^T\boldsymbol{A}[\boldsymbol{\psi}_1 \;\; \boldsymbol{\psi}_2], \tag{68}$$

$$\boldsymbol{C} = \begin{bmatrix} \boldsymbol{G}^T\boldsymbol{A} & \\ & \boldsymbol{G}^T\boldsymbol{A} \end{bmatrix}\begin{bmatrix} \boldsymbol{\psi}_1 & \\ & \boldsymbol{\psi}_2 \end{bmatrix}, \tag{69}$$

$$\boldsymbol{Q} = \boldsymbol{G}^T\boldsymbol{A}[\boldsymbol{\psi}_1 \;\; \boldsymbol{\psi}_2]\begin{bmatrix} \boldsymbol{\psi}_1^T & \\ & \boldsymbol{\psi}_2^T \end{bmatrix}\begin{bmatrix} \boldsymbol{A}^T\boldsymbol{G} & \\ & \boldsymbol{A}^T\boldsymbol{G} \end{bmatrix}. \tag{70}$$

Accordingly, the partial derivatives of $\boldsymbol{B}$ and $\boldsymbol{C}$ with respect to θ are given by

$$\acute{\boldsymbol{B}} = j\pi\cos(\theta)\boldsymbol{G}^T\boldsymbol{A}\boldsymbol{D}[\boldsymbol{\psi}_1 \;\; \boldsymbol{\psi}_2], \tag{71}$$

$$\acute{\boldsymbol{C}} = j\pi\cos(\theta)\begin{bmatrix} \boldsymbol{G}^T\boldsymbol{A}\boldsymbol{D} & \\ & \boldsymbol{G}^T\boldsymbol{A}\boldsymbol{D} \end{bmatrix}\begin{bmatrix} \boldsymbol{\psi}_1 & \\ & \boldsymbol{\psi}_2 \end{bmatrix}, \tag{72}$$

where $\boldsymbol{D} = \mathrm{diag}(0, 1\cdots, N-1)$. From the relationship $\boldsymbol{Q} = \boldsymbol{B}\boldsymbol{C}^T$, the derivative of $\boldsymbol{Q}$ with respect to θ is given by

$$\begin{aligned}\acute{\boldsymbol{Q}} =& \acute{\boldsymbol{B}}\boldsymbol{C}^T + \boldsymbol{B}\acute{\boldsymbol{C}}^T \\ =& j\pi\cos(\theta)\boldsymbol{G}^T\boldsymbol{A}\Bigg(\boldsymbol{D}[\boldsymbol{\psi}_1 \;\; \boldsymbol{\psi}_2]\begin{bmatrix} \boldsymbol{\psi}_1^T & \\ & \boldsymbol{\psi}_2^T \end{bmatrix} \\ &+ [\boldsymbol{\psi}_1 \;\; \boldsymbol{\psi}_2]\begin{bmatrix} \boldsymbol{\psi}_1^T\boldsymbol{D}^T & \\ & \boldsymbol{\psi}_2^T\boldsymbol{D}^T \end{bmatrix}\Bigg)\begin{bmatrix} \boldsymbol{A}^T\boldsymbol{G} & \\ & \boldsymbol{A}^T\boldsymbol{G} \end{bmatrix}.\end{aligned} \tag{73}$$

Recall that when $\mathrm{rank}(\boldsymbol{G}) = 1$, we have $\boldsymbol{G} = \sigma\boldsymbol{p}\boldsymbol{q}^H$. Define $\boldsymbol{F} \triangleq \boldsymbol{A}^H\boldsymbol{p}^*\boldsymbol{p}^T\boldsymbol{A} \in \mathbb{C}^{N\times N}$, $\mu_i \triangleq \boldsymbol{\psi}_i^H\boldsymbol{F}\boldsymbol{\psi}_i \in \mathbb{R}$, $\bar{\mu}_i \triangleq \boldsymbol{\psi}_i^H\boldsymbol{D}\boldsymbol{F}\boldsymbol{D}\boldsymbol{\psi}_i \in \mathbb{R}$, and $\tilde{\mu}_i \triangleq \boldsymbol{\psi}_i^H\boldsymbol{D}\boldsymbol{F}\boldsymbol{\psi}_i \in \mathbb{C}$. We have

$$\mathrm{tr}(\boldsymbol{Q}\boldsymbol{R}_x\boldsymbol{Q}^H) = \sigma^4(|\mu_1|^2 + |\mu_2|^2)|\boldsymbol{q}^H\boldsymbol{w}|^2, \tag{74}$$

$$\mathrm{tr}(\boldsymbol{Q}\boldsymbol{R}_x\acute{\boldsymbol{Q}}^H) = 2\sigma^4\pi\cos(\theta)(\mu_1\tilde{\mu}_1 + \mu_2\tilde{\mu}_2)|\boldsymbol{q}^H\boldsymbol{w}|^2, \tag{75}$$

$$\mathrm{tr}(\acute{\boldsymbol{Q}}\boldsymbol{R}_x\acute{\boldsymbol{Q}}^H) = 4\sigma^4\pi^2\cos^2(\theta)(\mu_1\bar{\mu}_1 + \mu_2\bar{\mu}_2)|\boldsymbol{q}^H\boldsymbol{w}|^2. \tag{76}$$

Substituting (74)–(76) into (15), the $\mathrm{CRB}(\theta)$ can be expressed as in (16). □

APPENDIX B
PROOF OF THEOREM 1

Proof. Suppose $f(\boldsymbol{x})$ is a continuously differentiable function with a convex domain, denoted as $\mathrm{dom}f$. Assume its gradient $\nabla f(\boldsymbol{x})$ is Lipschitz continuous with constant $L > 0$, i.e.,

$$\|\nabla f(\boldsymbol{x}) - \nabla f(\boldsymbol{y})\|_2 \leq L\|\boldsymbol{x} - \boldsymbol{y}\|_2, \tag{77}$$

for all $\boldsymbol{x}, \boldsymbol{y} \in \mathrm{dom}f$. By the generalized Cauchy-Schwarz inequality, we have

$$(\nabla f(\boldsymbol{x}) - \nabla f(\boldsymbol{y}))^T(\boldsymbol{x} - \boldsymbol{y}) \leq L\|\boldsymbol{x} - \boldsymbol{y}\|_2^2. \tag{78}$$

Since the domain of f is convex, for any $\boldsymbol{x}, \boldsymbol{y} \in \mathrm{dom}f$ and defining

$$r(t) = f(\boldsymbol{x} + t(\boldsymbol{y} - \boldsymbol{x})),\ t \in [0, 1], \tag{79}$$

we have $r(t) \in \mathrm{dom}f$. According to (78), we have

$$\begin{aligned} &r'(t) - r'(0) = \\ &\left(\nabla f(\boldsymbol{x} + t(\boldsymbol{y} - \boldsymbol{x})) - \nabla f(\boldsymbol{x})\right)^T(\boldsymbol{y} - \boldsymbol{x}) \leq tL\|\boldsymbol{y} - \boldsymbol{x}\|_2^2. \end{aligned} \tag{80}$$

Intergrating from $t = 0$ to $t = 1$ gives

$$\begin{aligned} f(\boldsymbol{y}) = r(1) =& r(0) + \int_0^1 r'(t)\, dt \\ \leq& r(0) + \int_0^1 r'(0) + tL\|\boldsymbol{y} - \boldsymbol{x}\|_2^2\, dt \\ =& r(0) + r'(0) + \frac{L}{2}\|\boldsymbol{y} - \boldsymbol{x}\|_2^2 \\ =& f(\boldsymbol{x}) + \nabla f(\boldsymbol{x})^T(\boldsymbol{y} - \boldsymbol{x}) + \frac{L}{2}\|\boldsymbol{y} - \boldsymbol{x}\|_2^2 \end{aligned} \tag{81}$$

Let $f_{\mathrm{ub}}(\boldsymbol{x}, \boldsymbol{y})$ denote the expression in the fourth line, i.e.,

$$f_{\mathrm{ub}}(\boldsymbol{x}, \boldsymbol{y}) \triangleq f(\boldsymbol{x}) + \nabla f(\boldsymbol{x})^T(\boldsymbol{y} - \boldsymbol{x}) + \frac{L}{2}\|\boldsymbol{y} - \boldsymbol{x}\|_2^2. \tag{82}$$

Then, $f_{\mathrm{ub}}(\boldsymbol{x}, \boldsymbol{y})$ serves as a quadratic upper bound for $f(\boldsymbol{y})$. □

APPENDIX C
DERIVATIONS OF THE GRADIENT OF $f(\boldsymbol{V}_1, \boldsymbol{V}_2)$

To facilitate the calculation of the gradient of $f(\boldsymbol{V}_1, \boldsymbol{V}_2)$, we reformulate $f(\boldsymbol{V}_1, \boldsymbol{V}_2)$ by decomposing it into the following two components:

$$f(\boldsymbol{V}_1, \boldsymbol{V}_2) = g(\boldsymbol{V}_1, \boldsymbol{V}_2) + h(\boldsymbol{V}_1, \boldsymbol{V}_2), \tag{83}$$

where

$$\begin{aligned} &g(\boldsymbol{V}_1, \boldsymbol{V}_2) \\ \triangleq& -\left(\mathrm{tr}(\boldsymbol{F}\boldsymbol{V}_1)\mathrm{tr}(\boldsymbol{D}\boldsymbol{F}\boldsymbol{D}\boldsymbol{V}_1) + \mathrm{tr}(\boldsymbol{F}\boldsymbol{V}_2)\mathrm{tr}(\boldsymbol{D}\boldsymbol{F}\boldsymbol{D}\boldsymbol{V}_2)\right), \end{aligned} \tag{84}$$

$$\begin{aligned} &h(\boldsymbol{V}_1, \boldsymbol{V}_2) \\ \triangleq& \frac{|\mathrm{tr}(\boldsymbol{F}\boldsymbol{V}_1)\mathrm{tr}(\boldsymbol{D}\boldsymbol{F}\boldsymbol{V}_1) + \mathrm{tr}(\boldsymbol{F}\boldsymbol{V}_2)\mathrm{tr}(\boldsymbol{D}\boldsymbol{F}\boldsymbol{V}_2)|^2}{\mathrm{tr}^2(\boldsymbol{F}\boldsymbol{V}_1) + \mathrm{tr}^2(\boldsymbol{F}\boldsymbol{V}_2)}. \end{aligned} \tag{85}$$

The gradient of $f(\boldsymbol{V}_1, \boldsymbol{V}_2)$ can be calculated as

$$\nabla f(\boldsymbol{V}_1, \boldsymbol{V}_2) = \begin{bmatrix} \frac{\partial f(\boldsymbol{V}_1, \boldsymbol{V}_2)}{\boldsymbol{V}_1} \\ \frac{\partial f(\boldsymbol{V}_1, \boldsymbol{V}_2)}{\boldsymbol{V}_2} \end{bmatrix}, \tag{86}$$

where

$$\frac{\partial f(\boldsymbol{V}_1, \boldsymbol{V}_2)}{\partial \boldsymbol{V}_1} = \frac{\partial g(\boldsymbol{V}_1, \boldsymbol{V}_2)}{\partial \boldsymbol{V}_1} + \frac{\partial h(\boldsymbol{V}_1, \boldsymbol{V}_2)}{\partial \boldsymbol{V}_1}, \tag{87}$$

$$\frac{\partial f(\boldsymbol{V}_1, \boldsymbol{V}_2)}{\partial \boldsymbol{V}_2} = \frac{\partial g(\boldsymbol{V}_1, \boldsymbol{V}_2)}{\partial \boldsymbol{V}_2} + \frac{\partial h(\boldsymbol{V}_1, \boldsymbol{V}_2)}{\partial \boldsymbol{V}_2}. \tag{88}$$

Define $\bar{\boldsymbol{F}} \triangleq \boldsymbol{D}\boldsymbol{F}\boldsymbol{D} \in \mathbb{C}^{N\times N}$, we have

$$\frac{\partial g(\boldsymbol{V}_1, \boldsymbol{V}_2)}{\partial \boldsymbol{V}_1} = -\boldsymbol{F}^T\mathrm{tr}(\bar{\boldsymbol{F}}\boldsymbol{V}_1) - \bar{\boldsymbol{F}}^T\mathrm{tr}(\boldsymbol{F}\boldsymbol{V}_1). \tag{89}$$

Define the numerator term of $h(\boldsymbol{V}_1, \boldsymbol{V}_2)$ as

$$\begin{aligned} &\mathrm{Num}_h(\boldsymbol{V}_1, \boldsymbol{V}_2) \\ \triangleq& |\mathrm{tr}(\boldsymbol{F}\boldsymbol{V}_1)\mathrm{tr}(\boldsymbol{D}\boldsymbol{F}\boldsymbol{V}_1) + \mathrm{tr}(\boldsymbol{F}\boldsymbol{V}_2)\mathrm{tr}(\boldsymbol{D}\boldsymbol{F}\boldsymbol{V}_2)|^2 \\ =& N_h N_h^*, \end{aligned} \tag{90}$$

where $N_h = \mathrm{tr}(\boldsymbol{F}\boldsymbol{V}_1)\mathrm{tr}(\boldsymbol{D}\boldsymbol{F}\boldsymbol{V}_1) + \mathrm{tr}(\boldsymbol{F}\boldsymbol{V}_2)\mathrm{tr}(\boldsymbol{D}\boldsymbol{F}\boldsymbol{V}_2) \in \mathbb{C}$ and $N_h^* = \mathrm{tr}(\boldsymbol{F}\boldsymbol{V}_1)\mathrm{tr}(\boldsymbol{F}\boldsymbol{D}\boldsymbol{V}_1) + \mathrm{tr}(\boldsymbol{F}\boldsymbol{V}_2)\mathrm{tr}(\boldsymbol{F}\boldsymbol{D}\boldsymbol{V}_2) \in \mathbb{C}$. Additionally, define the denominator term of $h(\boldsymbol{V}_1, \boldsymbol{V}_2)$ as

$$\mathrm{Den}_h(\boldsymbol{V}_1, \boldsymbol{V}_2) \triangleq \mathrm{tr}^2(\boldsymbol{F}\boldsymbol{V}_1) + \mathrm{tr}^2(\boldsymbol{F}\boldsymbol{V}_2) \in \mathbb{R}. \tag{91}$$

Then, the function $h(\boldsymbol{V}_1, \boldsymbol{V}_2)$ in (85) can be expressed as

$$h(\boldsymbol{V}_1, \boldsymbol{V}_2) = \frac{\mathrm{Num}_h(\boldsymbol{V}_1, \boldsymbol{V}_2)}{\mathrm{Den}_h(\boldsymbol{V}_1, \boldsymbol{V}_2)}. \tag{92}$$

Consequently, the partial derivative of $h(\boldsymbol{V}_1, \boldsymbol{V}_2)$ with respect to $\boldsymbol{V}_1$ is given by

$$\frac{\partial h(\boldsymbol{V}_1, \boldsymbol{V}_2)}{\partial \boldsymbol{V}_1} = \frac{\nabla_{\boldsymbol{V}_1}\mathrm{Num}_h \cdot \mathrm{Den}_h - \mathrm{Num}_h \cdot \nabla_{\boldsymbol{V}_1}\mathrm{Den}_h}{\mathrm{Den}_h^2}, \tag{93}$$

where the term $\nabla_{\boldsymbol{V}_1}\mathrm{Num}_h$ can be computed as follows

$$\nabla_{\boldsymbol{V}_1}\mathrm{Num}_h = \nabla_{\boldsymbol{V}_1}N_h \cdot N_h^* + \nabla_{\boldsymbol{V}_1}N_h^* \cdot N_h, \tag{94}$$

whose detials are omitted here for brevity, and

$$\nabla_{\boldsymbol{V}_1}\mathrm{Den}_h = 2\mathrm{tr}(\boldsymbol{F}\boldsymbol{V}_1)\boldsymbol{F}^T. \tag{95}$$

Using the result in (93), we can similarly derive the partial derivative of $f(\boldsymbol{V}_1, \boldsymbol{V}_2)$ with respect to $\boldsymbol{V}_2$, i.e., $\frac{\partial f(\boldsymbol{V}_1, \boldsymbol{V}_2)}{\partial \boldsymbol{V}_2}$.

APPENDIX D
PROOF OF PROPOSITION 2

Proof. Note that in (25), the domain of $\boldsymbol{V}_i, i \in \{1, 2\}$, denoted as $\mathrm{dom}\boldsymbol{V}$, is clearly convex. Based on Theorem 1, it suffices to demonstrate that the gradient of $f(\boldsymbol{V}_1, \boldsymbol{V}_2)$ is Lipschitz continuous. Specifically, we need to prove that for all $\boldsymbol{V}_1, \boldsymbol{V}_2 \in \mathrm{dom}\boldsymbol{V}$, there exists a constant $L > 0$ such that the following inequality holds:

$$\begin{aligned} &\|\nabla f(\boldsymbol{V}_1, \boldsymbol{V}_2) - \nabla f(\boldsymbol{W}_1, \boldsymbol{W}_2)\|_F \\ &\qquad \leq L\|(\boldsymbol{V}_1, \boldsymbol{V}_2) - (\boldsymbol{W}_1, \boldsymbol{W}_2)\|_F, \end{aligned} \tag{96}$$

where $\boldsymbol{W}_1$ and $\boldsymbol{W}_2$ are the counterparts of $\boldsymbol{V}_1$ and $\boldsymbol{V}_2$, respectively. Note $\boldsymbol{V}_1$ and $\boldsymbol{V}_2$ are symmetric in $f(\boldsymbol{V}_1, \boldsymbol{V}_2)$, so it suffices to prove that $\frac{\partial f(\boldsymbol{V}_1, \boldsymbol{V}_2)}{\boldsymbol{V}_1}$ is Lipschitz continuous. Let $\nabla_{\boldsymbol{V}_1}h(\boldsymbol{V}_1, \boldsymbol{V}_2)$ denote $\frac{\partial h(\boldsymbol{V}_1, \boldsymbol{V}_2)}{\partial \boldsymbol{V}_1}$ and $\nabla_{\boldsymbol{V}_1}g(\boldsymbol{V}_1, \boldsymbol{V}_2)$

$$
\begin{aligned}
&\|\nabla_{\boldsymbol{V}_1} h(\boldsymbol{V}_1,\boldsymbol{V}_2)-\nabla_{\boldsymbol{W}_1} h(\boldsymbol{W}_1,\boldsymbol{W}_2)\|_F\\
=&\left\|\frac{(\nabla_{\boldsymbol{V}_1}N_h\cdot N_h^*+\nabla_{\boldsymbol{V}_1}N_h^*\cdot N)D_h-|N_h|^2\cdot\nabla_{\boldsymbol{V}_1}D_h}{D_h^2}-\frac{(\nabla_{\boldsymbol{W}_1}M_h\cdot M_h^*+\nabla_{\boldsymbol{W}_1}M_h^*\cdot M)E_h-|M_h|^2\cdot\nabla_{\boldsymbol{W}_1}E_h}{E_h^2}\right\|_F\\
=&\left\|\frac{D_hN_h^*(\nabla_{\boldsymbol{V}_1}N_h-\nabla_{\boldsymbol{W}_1}M_h)+D_hN_h(\nabla_{\boldsymbol{V}_1}N_h^*-\nabla_{\boldsymbol{W}_1}M_h^*)}{D_h^2}\right.\\
&\left.+\frac{D_hN_h^*\nabla_{\boldsymbol{W}_1}M_h+D_hN_h\nabla_{\boldsymbol{W}_1}M_h^*}{D_h^2}-\frac{(\nabla_{\boldsymbol{W}_1}M_h\cdot M_h^*+\nabla_{\boldsymbol{W}_1}M_h^*\cdot M)E_h}{E_h^2}+\frac{|M_h|^2\cdot\nabla_{\boldsymbol{W}_1}E_h}{E_h^2}-\frac{|N_h|^2\cdot\nabla_{\boldsymbol{V}_1}D_h}{D_h^2}\right\|_F\\
\le&\underbrace{\left\|\frac{D_hN_h^*(\nabla_{\boldsymbol{V}_1}N_h-\nabla_{\boldsymbol{W}_1}M_h)+D_hN_h(\nabla_{\boldsymbol{V}_1}N_h^*-\nabla_{\boldsymbol{W}_1}M_h^*)}{D_h^2}\right\|_F}_{\text{(The first part.)}\triangleq\hbar_1}\\
&+\underbrace{\left\|\frac{D_hN_h^*\nabla_{\boldsymbol{W}_1}M_h+D_hN_h\nabla_{\boldsymbol{W}_1}M_h^*}{D_h^2}-\frac{(\nabla_{\boldsymbol{W}_1}M_h\cdot M_h^*+\nabla_{\boldsymbol{W}_1}M_h^*\cdot M)E_h}{E_h^2}\right\|_F}_{\text{(The second part.)}\triangleq\hbar_2}+\underbrace{\left\|\frac{|M_h|^2\cdot\nabla_{\boldsymbol{W}_1}E_h}{E_h^2}-\frac{|N_h|^2\cdot\nabla_{\boldsymbol{V}_1}D_h}{D_h^2}\right\|_F}_{\text{(The third part.)}\triangleq\hbar_3}
\end{aligned}
\tag{98}
$$

denote $\frac{\partial g(\boldsymbol{V}_1,\boldsymbol{V}_2)}{\partial \boldsymbol{V}_1}$. The gradient difference of the linear part in (87) can be calculated as

$$
\begin{aligned}
&\|\nabla_{\boldsymbol{V}_1} g(\boldsymbol{V}_1,\boldsymbol{V}_2)-\nabla_{\boldsymbol{W}_1} g(\boldsymbol{W}_1,\boldsymbol{W}_2)\|_F\\
=&\|-(\boldsymbol{F}^T\mathrm{tr}(\bar{\boldsymbol{F}}\boldsymbol{V}_1)+\bar{\boldsymbol{F}}^T\mathrm{tr}(\boldsymbol{F}\boldsymbol{V}_1))\\
&+(\boldsymbol{F}^T\mathrm{tr}(\bar{\boldsymbol{F}}\boldsymbol{W}_1)+\bar{\boldsymbol{F}}^T\mathrm{tr}(\boldsymbol{F}\boldsymbol{W}_1))\|_F\\
=&\|\bar{\boldsymbol{F}}^T\mathrm{tr}(\boldsymbol{F}\boldsymbol{W}_1)-\bar{\boldsymbol{F}}^T\mathrm{tr}(\boldsymbol{F}\boldsymbol{V}_1)\\
&+\boldsymbol{F}^T\mathrm{tr}(\bar{\boldsymbol{F}}\boldsymbol{W}_1)-\boldsymbol{F}^T\mathrm{tr}(\bar{\boldsymbol{F}}\boldsymbol{V}_1)\|_F\\
\le&\|\bar{\boldsymbol{F}}^T\mathrm{tr}(F(\boldsymbol{V}_1-\boldsymbol{W}_1))\|_F+\|\boldsymbol{F}^T\mathrm{tr}(\bar{\boldsymbol{F}}(\boldsymbol{V}_1-\boldsymbol{W}_1))\|_F\\
\le&2\|\bar{\boldsymbol{F}}^T\|_F\cdot\|\boldsymbol{F}^T\|_F\cdot\|\boldsymbol{V}_1-\boldsymbol{W}_1)\|_F\\
\triangleq&L_g\|\boldsymbol{V}_1-\boldsymbol{W}_1)\|_F,
\end{aligned}
\tag{97}
$$

where $\bar{\boldsymbol{F}}\triangleq\boldsymbol{D}\boldsymbol{F}\boldsymbol{D}$ and $L_g\triangleq 2\|\bar{\boldsymbol{F}}^T\|_F\cdot\|\boldsymbol{F}^T\|_F$. Clearly, the linear part of $\frac{\partial f(\boldsymbol{V}_1,\boldsymbol{V}_2)}{\boldsymbol{V}_1}$ is Lipschitz continuous. Next, we consider the fraction part in (87). For brevity, we define $D_h\triangleq\mathrm{Den}_h(\boldsymbol{V}_1,\boldsymbol{V}_2)$, $E_h\triangleq\mathrm{Den}_h(\boldsymbol{W}_1,\boldsymbol{W}_2)$ and $M_hM_h^*\triangleq\mathrm{Num}_h(\boldsymbol{W}_1,\boldsymbol{W}_2)$. The gradient difference of the fractional part in (87) can then be computed as shown in (98) at the top of this page. The first term in (98) is analyzed in (99), i.e.,

$$
\begin{aligned}
\hbar_1=&\left\|\frac{D_hN_h^*(\nabla_{\boldsymbol{V}_1}N_h-\nabla_{\boldsymbol{W}_1}M_h)+D_hN_h(\nabla_{\boldsymbol{V}_1}N_h^*-\nabla_{\boldsymbol{W}_1}M_h^*)}{D_h^2}\right\|_F\\
\le&\left\|\frac{N_h^*(\nabla_{\boldsymbol{V}_1}N_h-\nabla_{\boldsymbol{W}_1}M_h)}{D_h}\right\|_F+\left\|\frac{N_h(\nabla_{\boldsymbol{V}_1}N_h^*-\nabla_{\boldsymbol{W}_1}M_h^*)}{D_h}\right\|_F\\
=&\frac{|N_h|}{D_h}\cdot\big(\|\boldsymbol{F}^T\mathrm{tr}(\boldsymbol{D}\boldsymbol{F}(\boldsymbol{V}_1-\boldsymbol{W}_1))\\
&+(\boldsymbol{D}\boldsymbol{F})^T\mathrm{tr}(\boldsymbol{F}(\boldsymbol{V}_1-\boldsymbol{W}_1))\|_F\\
&+\|\boldsymbol{F}^T\mathrm{tr}(\boldsymbol{F}\boldsymbol{D}(\boldsymbol{V}_1-\boldsymbol{W}_1))\\
&+(\boldsymbol{F}\boldsymbol{D})^T\mathrm{tr}(\boldsymbol{F}(\boldsymbol{V}_1-\boldsymbol{W}_1))\|_F\big)\\
\le&4\tfrac{|N_h|}{D_h}\cdot\|\boldsymbol{F}\|_F\cdot\|\boldsymbol{F}\boldsymbol{D}\|_F\cdot\|\boldsymbol{V}_1-\boldsymbol{W}_1\|_F\\
\le&L_{h,1}\|\boldsymbol{V}_1-\boldsymbol{W}_1\|_F.
\end{aligned}
\tag{99}
$$

Note that in (99), $|N_h|$ has a positive upper bound, i.e., $0<|N_h|\le\varepsilon_N$, and $D_h\in\mathbb{R}$ has a positive lower bound, i.e., $D_h\ge\varepsilon_D>0$. Consequently, in (99) we can choose $L_{h,1}=4\frac{\varepsilon_N}{\varepsilon_D}\|\boldsymbol{F}\|_F\cdot\|\boldsymbol{F}\boldsymbol{D}\|_F$ so that the first term $\hbar_1$ in (98) is bounded.

Next, we analyze the second term $\hbar_2$ in (98). Note that

$$
\begin{aligned}
&\|N_h-M_h\|_F=\|N_h^*-M_h^*\|_F\\
&=\|\mathrm{tr}(\boldsymbol{F}\boldsymbol{V}_1)\mathrm{tr}(\boldsymbol{F}\boldsymbol{D}\boldsymbol{V}_1)+\mathrm{tr}(\boldsymbol{F}\boldsymbol{V}_2)\mathrm{tr}(\boldsymbol{F}\boldsymbol{D}\boldsymbol{V}_2)\\
&\quad-\mathrm{tr}(\boldsymbol{F}\boldsymbol{W}_1)\mathrm{tr}(\boldsymbol{F}\boldsymbol{D}\boldsymbol{W}_1)+\mathrm{tr}(\boldsymbol{F}\boldsymbol{W}_2)\mathrm{tr}(\boldsymbol{F}\boldsymbol{D}\boldsymbol{W}_2)\|_F\\
&=\|\mathrm{tr}(\boldsymbol{F}\boldsymbol{D}\boldsymbol{V}_1)(\mathrm{tr}(\boldsymbol{F}\boldsymbol{V}_1)-\mathrm{tr}(\boldsymbol{F}\boldsymbol{W}_1))\\
&\quad+\mathrm{tr}(\boldsymbol{F}\boldsymbol{W}_1)(\mathrm{tr}(\boldsymbol{F}\boldsymbol{D}\boldsymbol{V}_1)-\mathrm{tr}(\boldsymbol{F}\boldsymbol{D}\boldsymbol{W}_1))\\
&\quad+\mathrm{tr}(\boldsymbol{F}\boldsymbol{D}\boldsymbol{V}_2)(\mathrm{tr}(\boldsymbol{F}\boldsymbol{V}_2)-\mathrm{tr}(\boldsymbol{F}\boldsymbol{W}_2))\\
&\quad+\mathrm{tr}(\boldsymbol{F}\boldsymbol{W}_2)(\mathrm{tr}(\boldsymbol{F}\boldsymbol{D}\boldsymbol{V}_2)-\mathrm{tr}(\boldsymbol{F}\boldsymbol{D}\boldsymbol{W}_2))\|_F\\
&\le|\mathrm{tr}(\boldsymbol{F}\boldsymbol{D}\boldsymbol{V}_1)|\cdot\|\boldsymbol{F}\|_F\cdot\|\boldsymbol{V}_1-\boldsymbol{W}_1\|_F\\
&\quad+|\mathrm{tr}(\boldsymbol{F}\boldsymbol{W}_1)|\cdot\|\boldsymbol{F}\boldsymbol{D}\|_F\cdot\|\boldsymbol{V}_1-\boldsymbol{W}_1\|_F\\
&\quad+|\mathrm{tr}(\boldsymbol{F}\boldsymbol{D}\boldsymbol{V}_2)|\cdot\|\boldsymbol{F}\|_F\cdot\|\boldsymbol{V}_2-\boldsymbol{W}_2\|_F\\
&\quad+|\mathrm{tr}(\boldsymbol{F}\boldsymbol{W}_2)|\cdot\|\boldsymbol{F}\boldsymbol{D}\|_F\cdot\|\boldsymbol{V}_2-\boldsymbol{W}_2\|_F,
\end{aligned}
\tag{100}
$$

and

$$
\begin{aligned}
&\|D_h-E_h\|_F\\
=&\|\mathrm{tr}^2(\boldsymbol{F}\boldsymbol{V}_1)+\mathrm{tr}^2(\boldsymbol{F}\boldsymbol{V}_2)-\mathrm{tr}^2(\boldsymbol{F}\boldsymbol{W}_1)+\mathrm{tr}^2(\boldsymbol{F}\boldsymbol{W}_2)\|_F\\
=&\|(\mathrm{tr}(\boldsymbol{F}\boldsymbol{V}_1)+\mathrm{tr}(\boldsymbol{F}\boldsymbol{W}_1))\cdot(\mathrm{tr}(\boldsymbol{F}\boldsymbol{V}_1)-\mathrm{tr}(\boldsymbol{F}\boldsymbol{W}_1))\\
&+(\mathrm{tr}(\boldsymbol{F}\boldsymbol{V}_2)+\mathrm{tr}(\boldsymbol{F}\boldsymbol{W}_2))\cdot(\mathrm{tr}(\boldsymbol{F}\boldsymbol{V}_2)-\mathrm{tr}(\boldsymbol{F}\boldsymbol{W}_2))\|_F\\
\le&|\mathrm{tr}(\boldsymbol{F}\boldsymbol{V}_1)+\mathrm{tr}(\boldsymbol{F}\boldsymbol{W}_1)|\cdot\|\boldsymbol{F}\|_F\cdot\|\boldsymbol{V}_1-\boldsymbol{W}_1\|_F\\
&+|\mathrm{tr}(\boldsymbol{F}\boldsymbol{V}_2)+\mathrm{tr}(\boldsymbol{F}\boldsymbol{W}_2)|\cdot\|\boldsymbol{F}\|_F\cdot\|\boldsymbol{V}_2-\boldsymbol{W}_2\|_F.
\end{aligned}
\tag{101}
$$

Then, we can express the second term $\hbar_2$ as shown in (102) at the top of the next page. Note that $\|\nabla_{\boldsymbol{W}_1}M_h\|_F=\|\boldsymbol{F}^T\mathrm{tr}(\boldsymbol{D}\boldsymbol{F}\boldsymbol{W}_1)+(\boldsymbol{D}\boldsymbol{F})^T\mathrm{tr}(\boldsymbol{F}\boldsymbol{W}_1)\|_F$ has a positive upper bound, which enables us to determine $L_{h,2}$ in (102). Consequently, we can conclude that second term $\hbar_2$ in (98) is bounded.

The third term, $\hbar_3$, in (98) is given by (103), as shown at the top of the next page. Similarly, since $\|\nabla_{\boldsymbol{W}_1}E_h\|_F=\|2\mathrm{tr}(\boldsymbol{F}\boldsymbol{V}_1)\boldsymbol{F}^T\|_F$ has a positive upper bound, the constant $L_{h,3}$ in (103) can also be determined. This ensures that the third term $\hbar_3$ in (98) is bounded.

Based on (99)–(103), we can conclude that the fraction part in (87) is Lipschitz continuous,i.e.,

$$
\begin{aligned}
&\|\nabla_{\boldsymbol{V}_1} h(\boldsymbol{V}_1,\boldsymbol{V}_2)-\nabla_{\boldsymbol{W}_1} h(\boldsymbol{W}_1,\boldsymbol{W}_2)\|_F\\
\le&(L_{h,1}+L_{h,2}+L_{h,3})\|(\boldsymbol{V}_1,\boldsymbol{V}_2)-(\boldsymbol{W}_1,\boldsymbol{W}_2)\|_F.
\end{aligned}
\tag{104}
$$

$$
\begin{aligned}
\hbar_2 =& \left\| \frac{D_h N_h^* \nabla_{\boldsymbol{W}_1} M_h + D_h N_h \nabla_{\boldsymbol{W}_1} M_h^*}{D_h^2} - \frac{(\nabla_{\boldsymbol{W}_1} M_h \cdot M_h^* + \nabla_{\boldsymbol{W}_1} M_h^* \cdot M) E_h}{E_h^2} \right\|_F \\
\leq& \left\| \frac{(N_h^* - M_h^*) \nabla_{\boldsymbol{W}_1} M_h}{D_h} + \frac{M_h^* \nabla_{\boldsymbol{W}_1} M_h}{D_h} - \frac{M_h^* \nabla_{\boldsymbol{W}_1} M_h}{E_h} \right\|_F + \left\| \frac{(N_h - M_h) \nabla_{\boldsymbol{W}_1} M_h^*}{D_h} + \frac{M_h \nabla_{\boldsymbol{W}_1} M_h^*}{D_h} - \frac{M_h \nabla_{\boldsymbol{W}_1} M_h^*}{E_h} \right\|_F \\
\leq& \left\| \frac{\nabla_{\boldsymbol{W}_1} M_h}{D_h} \right\|_F \cdot \|N_h^* - M_h^*\|_F + \left\| \frac{M_h^* \nabla_{\boldsymbol{W}_1} M_h}{D_h E_h} \right\|_F \cdot \|D_h - E_h\|_F \\
&+ \left\| \frac{\nabla_{\boldsymbol{W}_1} M_h^*}{D_h} \right\|_F \cdot \|N_h - M_h\|_F + \left\| \frac{M_h \nabla_{\boldsymbol{W}_1} M_h^*}{D_h E_h} \right\|_F \cdot \|D_h - E_h\|_F \\
=& 2 \left\| \frac{\nabla_{\boldsymbol{W}_1} M_h}{D_h} \right\|_F \cdot \|N_h^* - M_h^*\|_F + 2 \left\| \frac{M_h^* \nabla_{\boldsymbol{W}_1} M_h}{D_h E_h} \right\|_F \cdot \|D_h - E_h\|_F \\
\leq& 2 \left\| \frac{\nabla_{\boldsymbol{W}_1} M_h}{D_h} \right\|_F (|\mathrm{tr}(\boldsymbol{F}\boldsymbol{D}\boldsymbol{V}_1)| \cdot \|\boldsymbol{F}\|_F + |\mathrm{tr}(\boldsymbol{F}\boldsymbol{W}_1)| \cdot \|\boldsymbol{F}\boldsymbol{D}\|_F) \cdot \|\boldsymbol{V}_1 - \boldsymbol{W}_1\|_F \\
&+ 2 \left\| \frac{M_h^* \nabla_{\boldsymbol{W}_1} M_h}{D_h E_h} \right\|_F \cdot |\mathrm{tr}(\boldsymbol{F}\boldsymbol{V}_1) + \mathrm{tr}(\boldsymbol{F}\boldsymbol{W}_1)| \cdot \|\boldsymbol{F}\|_F \cdot \|\boldsymbol{V}_1 - \boldsymbol{W}_1\|_F \\
&+ 2 \left\| \frac{\nabla_{\boldsymbol{W}_1} M_h}{D_h} \right\|_F \cdot (|\mathrm{tr}(\boldsymbol{F}\boldsymbol{D}\boldsymbol{V}_2)| \cdot \|\boldsymbol{F}\|_F + |\mathrm{tr}(\boldsymbol{F}\boldsymbol{W}_2)| \cdot \|\boldsymbol{F}\boldsymbol{D}\|_F) \cdot \|\boldsymbol{V}_2 - \boldsymbol{W}_2\|_F \\
&+ 2 \left\| \frac{M_h^* \nabla_{\boldsymbol{W}_1} M_h}{D_h E_h} \right\|_F \cdot |\mathrm{tr}(\boldsymbol{F}\boldsymbol{V}_2) + \mathrm{tr}(\boldsymbol{F}\boldsymbol{W}_2)| \cdot \|\boldsymbol{F}\|_F \cdot \|\boldsymbol{V}_2 - \boldsymbol{W}_2\|_F \\
\leq& L_{h,2} \|(\boldsymbol{V}_1, \boldsymbol{V}_2) - (\boldsymbol{W}_1, \boldsymbol{W}_2)\|_F
\end{aligned} \tag{102}
$$

$$
\begin{aligned}
\hbar_3 =& \left\| \frac{|M_h|^2 \cdot \nabla_{\boldsymbol{W}_1} E_h}{E_h^2} - \frac{|N_h|^2 \cdot \nabla_{\boldsymbol{V}_1} D_h}{D_h^2} \right\|_F \\
=& \left\|_F \frac{|N_h|^2 \cdot \nabla_{\boldsymbol{V}_1} D_h - |N_h|^2 \cdot \nabla_{\boldsymbol{W}_1} E_h}{D_h^2} + \frac{|N_h|^2 \cdot \nabla_{\boldsymbol{W}_1} E_h}{D_h^2} - \frac{|M_h|^2 \cdot \nabla_{\boldsymbol{W}_1} E_h}{E_h^2} \right\|_F \\
\leq& \left\| \frac{|N_h|^2}{D_h^2} \right\|_F \cdot \|\nabla_{\boldsymbol{V}_1} D_h - \nabla_{\boldsymbol{W}_1} E_h\|_F + \left\| \frac{\nabla_{\boldsymbol{W}_1} E_h}{D_h^2} \right\|_F \cdot \||N_h|^2 - |M_h|^2\|_F + \left\| \frac{|M_h|^2 \nabla_{\boldsymbol{W}_1} E_h}{D_h^2 E_h^2} \right\|_F \cdot \|E_h^2 - D_h^2\|_F \\
=& \left\| \frac{|N_h|^2}{D_h^2} \right\|_F \cdot 2\|\mathrm{tr}(\boldsymbol{F}\boldsymbol{V}_1)\boldsymbol{F}^T - \mathrm{tr}(\boldsymbol{F}\boldsymbol{W}_1)\boldsymbol{F}^T\|_F + \left\| \frac{\nabla_{\boldsymbol{W}_1} E_h}{D_h^2} \right\|_F \cdot \|\Re((N_h - M_h)(N_h + M_h)^*)\|_F \\
&+ \left\| \frac{|M_h|^2 \nabla_{\boldsymbol{W}_1} E_h}{D_h^2 E_h^2} \right\|_F \cdot \|(D_h - E_h)(D_h + E_h)\|_F \\
\leq& 2 \left\| \frac{|N_h|^2}{D_h^2} \right\|_F \cdot \|\boldsymbol{F}\|_F^2 \cdot \|\boldsymbol{V}_1 - \boldsymbol{W}_1\|_F \\
&+ \left\| \frac{\nabla_{\boldsymbol{W}_1} E_h}{D_h^2} \right\|_F \cdot |N_h + M_h| \cdot \|N_h - M_h\|_F + \left\| \frac{|M_h|^2 \nabla_{\boldsymbol{W}_1} E_h}{D_h^2 E_h^2} \right\|_F \cdot |D_h + E_h| \cdot \|D_h - E_h\|_F \\
\leq& L_{h,3} \|(\boldsymbol{V}_1, \boldsymbol{V}_2) - (\boldsymbol{W}_1, \boldsymbol{W}_2)\|_F
\end{aligned} \tag{103}
$$

Based on (97) and (104), we can conclude that

$$
\begin{aligned}
&\|\nabla_{\boldsymbol{V}_1} h(\boldsymbol{V}_1, \boldsymbol{V}_2) - \nabla_{\boldsymbol{W}_1} h(\boldsymbol{W}_1, \boldsymbol{W}_2)\|_F \\
&\qquad \leq L_1 \|(\boldsymbol{V}_1, \boldsymbol{V}_2) - (\boldsymbol{W}_1, \boldsymbol{W}_2)\|_F.
\end{aligned} \tag{105}
$$

where L_1 can be chosen as $L_1 = L_g + L_{h,1} + L_{h,2} + L_{h,3}$. Hence, $\frac{\partial f(\boldsymbol{V}_1, \boldsymbol{V}_2)}{\boldsymbol{V}_1}$ is Lipschitz continuous. □

REFERENCES

[1] F. Liu, Y. Cui, C. Masouros, J. Xu, T. X. Han, Y. C. Eldar, and S. Buzzi, "Integrated sensing and communications: Toward dual-functional wireless networks for 6G and beyond," *IEEE Journal on Selected Areas in Communications*, vol. 40, no. 6, pp. 1728–1767, 2022.

[2] F. Liu, C. Masouros, A. P. Petropulu, H. Griffiths, and L. Hanzo, "Joint radar and communication design: Applications, state-of-the-art, and the road ahead," *IEEE Transactions on Communications*, vol. 68, no. 6, pp. 3834–3862, 2020.

[3] J. A. Zhang, F. Liu, C. Masouros, R. W. Heath, Z. Feng, L. Zheng, and A. Petropulu, "An overview of signal processing techniques for joint communication and radar sensing," *IEEE Journal of Selected Topics in Signal Processing*, vol. 15, no. 6, pp. 1295–1315, 2021.

[4] Z. Wei, F. Liu, C. Masouros, N. Su, and A. P. Petropulu, "Toward multi-functional 6G wireless networks: Integrating sensing, communication, and security," *IEEE Communications Magazine*, vol. 60, no. 4, pp. 65–71, 2022.

[5] Q. Wu and R. Zhang, "Intelligent reflecting surface enhanced wireless network via joint active and passive beamforming," *IEEE Transactions on Wireless Communications*, vol. 18, no. 11, pp. 5394–5409, 2019.

[6] M. Di Renzo, A. Zappone, M. Debbah, M.-S. Alouini, C. Yuen, J. de Rosny, and S. Tretyakov, "Smart radio environments empowered by reconfigurable intelligent surfaces: How it works, state of research, and the road ahead," *IEEE Journal on Selected Areas in Communications*, vol. 38, no. 11, pp. 2450–2525, 2020.

[7] Q. Wu and R. Zhang, "Towards smart and reconfigurable environment: Intelligent reflecting surface aided wireless network," *IEEE Communications Magazine*, vol. 58, no. 1, pp. 106–112, 2020.

[8] C. Luo, J. Hu, L. Xiang, and K. Yang, "Reconfigurable intelligent sensing surface aided wireless powered communication networks: A sensing-then-reflecting approach," *IEEE Transactions on Communications*, vol. 72, no. 3, pp. 1835–1848, 2024.

[9] M. Hua, Q. Wu, W. Chen, Z. Fei, H. C. So, and C. Yuen, "Intelligent reflecting surface-assisted localization: Performance analysis and algorithm design," *IEEE Wireless Communications Letters*, vol. 13, no. 1, pp. 84–88, 2024.

[10] M. Hua, G. Chen, K. Meng, S. Ma, C. Yuen, and H. Cheung So, "3D multi-target localization via intelligent reflecting surface: Protocol and analysis," *IEEE Transactions on Wireless Communications*, vol. 23,

no. 11, pp. 16 527–16 543, 2024.
[11] S. Buzzi, E. Grossi, M. Lops, and L. Venturino, "Foundations of MIMO radar detection aided by reconfigurable intelligent surfaces," *IEEE Transactions on Signal Processing*, vol. 70, pp. 1749–1763, 2022.
[12] F. Wang, H. Li, and J. Fang, "Joint active and passive beamforming for IRS-assisted radar," *IEEE Signal Processing Letters*, vol. 29, pp. 349–353, 2022.
[13] Z. Esmaeilbeig, A. Eamaz, K. V. Mishra, and M. Soltanalian, "Moving target detection via multi-IRS-aided OFDM radar," in *2023 IEEE Radar Conference (RadarConf23)*, 2023, pp. 1–6.
[14] M. K. Ercan, A. Pourafzal, M. F. Keskin, and et al., "RIS-aided NLoS monostatic multi-target sensing under angle-doppler coupling," *TechRxiv*, October 2024.
[15] X. Shao, C. You, W. Ma, X. Chen, and R. Zhang, "Target sensing with intelligent reflecting surface: Architecture and performance," *IEEE Journal on Selected Areas in Communications*, vol. 40, no. 7, pp. 2070–2084, 2022.
[16] Z. Esmaeilbeig, K. V. Mishra, and M. Soltanalian, "IRS-aided radar: Enhanced target parameter estimation via intelligent reflecting surfaces," in *2022 IEEE 12th Sensor Array and Multichannel Signal Processing Workshop (SAM)*, 2022, pp. 286–290.
[17] Z. Yu, X. Hu, C. Liu, Q. Tao, and M. Peng, "Detection and multi-parameter estimation for NLOS targets: An IRS-assisted framework," 2024. [Online]. Available: https://arxiv.org/abs/2407.03902
[18] F. Wen, J. Shi, G. Gui, C. Yuen, H. Sari, and F. Adachi, "Joint DOD and DOA estimation for NLOS target using IRS-aided bistatic MIMO radar," *IEEE Transactions on Vehicular Technology*, vol. 73, no. 10, pp. 15 798–15 802, 2024.
[19] J. Wang, J. Fang, H. Li, and L. Huang, "Intelligent reflecting surface-assisted NLOS sensing with OFDM signals," *IEEE Transactions on Signal Processing*, vol. 72, pp. 5322–5337, 2024.
[20] X. Song, J. Xu, F. Liu, T. X. Han, and Y. C. Eldar, "Intelligent reflecting surface enabled sensing: Cramér-rao bound optimization," *IEEE Transactions on Signal Processing*, vol. 71, pp. 2011–2026, 2023.
[21] Z. Esmaeilbeig, A. Eamaz, K. V. Mishra, and M. Soltanalian, "Joint waveform and passive beamformer design in multi-IRS-aided radar," in *ICASSP 2023 - 2023 IEEE International Conference on Acoustics, Speech and Signal Processing (ICASSP)*, 2023, pp. 1–5.
[22] Q. Peng, Q. Wu, W. Chen, S. Ma, M.-M. Zhao, and O. A. Dobre, "Semi-passive intelligent reflecting surface-enabled sensing systems," *IEEE Transactions on Communications*, vol. 72, no. 12, pp. 7674–7688, 2024.
[23] X. Shao, C. You, and R. Zhang, "Intelligent reflecting surface aided wireless sensing: Applications and design issues," *IEEE Wireless Communications*, pp. 1–7, 2024.
[24] Z. Yu, X. Hu, C. Liu, M. Peng, and C. Zhong, "Location sensing and beamforming design for IRS-enabled multi-user ISAC systems," *IEEE Transactions on Signal Processing*, vol. 70, pp. 5178–5193, 2022.
[25] C. Liao, F. Wang, and V. K. N. Lau, "Optimized design for IRS-assisted integrated sensing and communication systems in clutter environments," *IEEE Transactions on Communications*, vol. 71, no. 8, pp. 4721–4734, 2023.
[26] E. Shtaiwi, H. Zhang, A. Abdelhadi, A. L. Swindlehurst, Z. Han, and H. V. Poor, "Sum-rate maximization for RIS-assisted integrated sensing and communication systems with manifold optimization," *IEEE Transactions on Communications*, vol. 71, no. 8, pp. 4909–4923, 2023.
[27] Y. Fang, S. Zhang, X. Li, X. Yu, J. Xu, and S. Cui, "Multi-IRS-enabled integrated sensing and communications," *IEEE Transactions on Communications*, vol. 72, no. 9, pp. 5853–5867, 2024.
[28] F. Liu, Y.-F. Liu, A. Li, C. Masouros, and Y. C. Eldar, "Cramér-rao bound optimization for joint radar-communication beamforming," *IEEE Transactions on Signal Processing*, vol. 70, pp. 240–253, 2022.
[29] M. R. Akdeniz, Y. Liu, M. K. Samimi, S. Sun, S. Rangan, T. S. Rappaport, and E. Erkip, "Millimeter wave channel modeling and cellular capacity evaluation," *IEEE Journal on Selected Areas in Communications*, vol. 32, no. 6, pp. 1164–1179, 2014.
[30] S. Sun, T. S. Rappaport, M. Shafi, P. Tang, J. Zhang, and P. J. Smith, "Propagation models and performance evaluation for 5G millimeter-wave bands," *IEEE Transactions on Vehicular Technology*, vol. 67, no. 9, pp. 8422–8439, 2018.
[31] E. Ben-Dor, T. S. Rappaport, Y. Qiao, and S. J. Lauffenburger, "Millimeter-wave 60 GHz outdoor and vehicle AOA propagation measurements using a broadband channel sounder," in *2011 IEEE Global Telecommunications Conference - GLOBECOM 2011*, 2011, pp. 1–6.
[32] Z. Gao, L. Dai, D. Mi, Z. Wang, M. A. Imran, and M. Z. Shakir, "Mmwave massive-MIMO-based wireless backhaul for the 5G ultra-dense network," *IEEE Wireless Communications*, vol. 22, no. 5, pp. 13–21, 2015.
[33] M. Lübke, J. Fuchs, A. Dubey, H. Hamoud, F. Dressler, R. Weigel, and F. Lurz, "Validation and analysis of the propagation channel at 60 GHz for vehicular communication," in *2021 IEEE 94th Vehicular Technology Conference (VTC2021-Fall)*, 2021, pp. 1–7.
[34] G. Zhou, C. Pan, H. Ren, K. Wang, and A. Nallanathan, "A framework of robust transmission design for IRS-aided MISO communications with imperfect cascaded channels," *IEEE Transactions on Signal Processing*, vol. 68, pp. 5092–5106, 2020.
[35] Y. Zhang, W. Ni, J. Wang, W. Tang, M. Jia, Y. C. Eldar, and D. Niyato, "Robust transceiver design for covert integrated sensing and communications with imperfect CSI," *IEEE Transactions on Communications*, pp. 1–1, 2024.

Jilin Wang (Graduate Student Member, IEEE) received the B.Eng. degree from Tiangong University, Tianjin, China, in 2019. He is currently pursuing the Ph.D. degree with the National Key Laboratory of Wireless Communications, University of Electronic Science and Technology of China, Chengdu, China, and is a visiting Ph.D. student with the Department of Electronic and Electrical Engineering, University College London, London, U.K. His research interests include millimeter-wave communications, signal processing, and integrated sensing and communications (ISAC).

Jun Fang (SM'19) received the B.S. and M.S. degrees from the Xidian University, Xi'an, China in 1998 and 2001, respectively, and the Ph.D. degree from the National University of Singapore, Singapore, in 2006, all in electrical engineering.

During 2006, he was a postdoctoral research associate in the Department of Electrical and Computer Engineering, Duke University. From January 2007 to December 2010, he was a research associate with the Department of Electrical and Computer Engineering, Stevens Institute of Technology. Since 2011, he has been with the University of Electronic of Science and Technology of China, where he is currently a Professor. His research interests include compressed sensing and sparse theory, massive MIMO/mmWave communications, and statistical inference.

Dr. Fang received the 2013 and 2025 IEEE Jack Neubauer Memorial Awards for the best systems papers published in the *IEEE Transactions on Vehicular Technology*, and received the 2024 IEEE Signal Process. Lett. Best Paper Award. He served as an Associate Technical Editor for *IEEE Communications Magazine* from 2012 to 2020, and a Senior Associate Editor for *IEEE Signal Processing Letters* from 2018 to 2022. He is currently an Associate Editor for *IEEE Transactions on Vehicular Technology*, and a Member of the IEEE SPS Sensor Array and Multichannel TC.

Hongbin Li (M'99-SM'08-F'19) received the B.S. and M.S. degrees from the University of Electronic Science and Technology of China, in 1991 and 1994, respectively, and the Ph.D. degree from the University of Florida, Gainesville, FL, in 1999, all in electrical engineering.

From July 1996 to May 1999, he was a Research Assistant in the Department of Electrical and Computer Engineering at the University of Florida. Since July 1999, he has been with the Department of Electrical and Computer Engineering, Stevens Institute of Technology, Hoboken, NJ, where he is currently the Charles and Rosanna Batchelor Memorial Chair Professor. He was a Summer Visiting Faculty Member at the Air Force Research Laboratory in the summers of 2003, 2004 and 2009. His general research interests include statistical signal processing, wireless communications, and radars.

Dr. Li received a number of awards including the IEEE Jack Neubauer Memorial Award in 2013, Master of Engineering (Honoris Causa) from Stevens Institute of Technology in 2024, Provost's Award for Research Excellence in 2019, Harvey N. Davis Teaching Award in 2003, and Jess H. Davis Memorial Research Award in 2001, and Sigma Xi Graduate Research Award in 1999. He has been a member of the IEEE SPS Signal Processing Theory and Methods Technical Committee (TC) and the IEEE SPS Sensor Array and Multichannel TC, an Associate Editor for *Signal Processing* (Elsevier), *IEEE Transactions on Signal Processing*, *IEEE Signal Processing Letters*, and *IEEE Transactions on Wireless Communications*, as well as a Guest Editor for *IEEE Journal of Selected Topics in Signal Processing* and *EURASIP Journal on Applied Signal Processing*. He has been involved in various conference organization activities, including serving as a General Co-Chair for the 7th IEEE Sensor Array and Multichannel Signal Processing (SAM) Workshop, Hoboken, NJ, June 17-20, 2012. Dr. Li is a member of Tau Beta Pi and Phi Kappa Phi, and a fellow of the Asia-Pacific Artificial Intelligence Association (AAIA) and the International Artificial Intelligence Industry Alliance (AIIA).

Christos Masouros (Fellow, IEEE) received the Diploma degree in electrical and computer engineering from the University of Patras, Greece, in 2004, and the M.Sc. by research and Ph.D. degrees in electrical and electronic engineering from The University of Manchester, U.K., in 2006 and 2009, respectively.

In 2008, he was a Research Intern at Philips Research Labs, U.K. Between 2009 and 2010, he was a Research Associate with The University of Manchester, and from 2010 to 2012, he was a Research Fellow at Queen's University Belfast. In 2012, he joined University College London as a Lecturer. He held a Royal Academy of Engineering Research Fellowship between 2011 and 2016. Since 2019, he has been a Full Professor of signal processing and wireless communications with the Information and Communication Engineering Research Group, Department of Electrical and Electronic Engineering, and is affiliated with the Institute for Communications and Connected Systems, University College London. His research interests lie in the field of wireless communications and signal processing with particular focus on green communications, large-scale antenna systems, integrated sensing and communications (ISAC), interference mitigation techniques for MIMO, and multicarrier communications.

He was the co-recipient of the 2021 IEEE SPS Young Author Best Paper Award, and the recipient of the Best Paper Awards at IEEE GlobeCom 2015 and IEEE WCNC 2019. He has been recognized as an Exemplary Editor for IEEE Communications Letters and as an Exemplary Reviewer for IEEE Transactions on Communications. He is a founding member and the Vice-Chair of the IEEE Emerging Technology Initiative on ISAC, the Vice-Chair of the IEEE Special Interest Group on ISAC, and the Chair of the IEEE Special Interest Group on Energy Harvesting Communication Networks. He is an Editor of IEEE Transactions on Communications, IEEE Transactions on Wireless Communications, IEEE Open Journal of Signal Processing, and the Editor-at-Large of IEEE Open Journal of the Communications Society. He was an Associate Editor of IEEE Communications Letters and a Guest Editor for a number of special issues in IEEE Journal of Selected Topics in Signal Processing and IEEE Journal on Selected Areas in Communications.